

# Chapter1

## Introduction

### 1.1 Liquid Crystal Binary Phase Grating

Recently, various liquid crystal phase gratings have been developed and expected to be applied in the applications of projection displays [1-2], optical communication, polarization beam splitters, optical switching, controlled focusing by voltage and photonic liquid crystal devices [3-4]. Liquid crystal gratings have advantages of low voltage, low power consumption, low cost and compactness. Depending on the liquid crystal material used and on modulator geometry, electro-optic modulation of phase, any states of polarization corresponding to refractive index are controlled and the phase retardation can control transforms of polarization states. Several methods of developing LC diffractive gratings are proposed such as patterned photo-polymerization, patterned electrodes and holographic alignment techniques [5-7].

In the past, two problems still remain unsolved: (1) complicated fabrication and (2) slow response time. In this study, a simple phase grating fabrication method using ITO (indium tin oxide) etched pattern was proposed. Ferroelectric liquid crystals were proposed to solve the slow response time of nematic liquid crystal device in previous study [8].

## 1.2 Liquid Crystal Phase

Liquid crystal is a state of matter that is intermediate between the crystalline solid and the amorphous liquid. It may also be viewed as a liquid in which an ordered arrangement of molecules exists. Liquid crystals arise under certain conditions in organic substance having sharply anisotropic molecules, that is, highly elongated (rod-like) molecules or flat (disc-like) molecules. Thus, a direct consequence resulted from the ordering of anisotropic molecules is the anisotropy of mechanical, electric, magnetic and optical properties.

There are many types of liquid crystals, according to the structure of material. Even though the shapes of molecules are complicated, often they are referred to as rod-like. Other shapes (discotic-like or sanidic-like) of molecules are not our interest in this thesis.



### Nematic

The nematic liquid crystal phase is characterized by molecules that has no positional order but has tenancy to point toward a same direction (parallel to director, indicated by  $n$ ). In nematic phase only the long axis of molecule is more or less oriented, therefore it is optically uniaxial. The measurement of the degree of order in nematic phase is given by the so-called order parameter

$$S = \left\langle \frac{3}{2} \cos^2 \omega - \frac{1}{2} \right\rangle \quad (1.1)$$

where  $\omega$  is the deviation angle of each molecule from the director. If  $S=0$ , the substance is in isotropic phase (randomly ordered);  $S=1$ , the substance is in solid state (perfectly ordered). Typically, liquid crystal has  $0.5 < S < 0.7$ .

## **Chiral Nematic**

The chiral nematic (or cholesteric) liquid crystal phase is typically composed of nematic mesogenic molecules which contains a chiral center. Usually when we mix chiral dopants with achiral nematic liquid crystal, a chiral nematic liquid crystal is formed. The chirality produces an intermolecular force that leads to a twist between each layer. As a result the director in  $N^*$  phase not only oriented uniformly in individual layer but also rotates in space about a helical axis, which is perpendicular to the layer plane. An important characteristic of chiral nematic liquid crystal is the pitch. The pitch,  $p$ , is defined as the distance it takes for the director to rotate a full turn in the helix, and it strongly depends on the concentration of chiral dopants in the mixture. The pitch typically varies between a few hundred nanometers and many micrometers.

The helical structure of chiral nematic phase has the ability to selectively reflect light of wavelength equals to helical pitch in  $N^*$  of the material. The pitch length also depends on temperature, for example: If we increase the temperature the pitch will be tighter and we will see bluish color (or shorter wavelength of light) be reflected; if we decrease the temperature the pitch will be loosened and yellowish color (or longer wavelength of light) will be reflected.

## **Smectic**

Material in the smectic phase shows an additional degree of positional order not present in nematic phase, which means molecules are ordered in layers (smectic layers). Motion of molecules is restricted to within these layers, and adjacent layers are observed to flow past each other. In smectic A phase, the layer spacing approximately equals to the length of molecule. In smectic C phase, molecules are arranged in layers as in smectic A phase, but the directors are tilted in a preferred

angle respect to the layer normal. This indicates that the molecule is confined to a conical surface of which layer normal is the axis, and the cone is the so-called smectic cone. Because the molecules tilt when material entering SmC phase from SmA phase, the layer spacing in SmC phase would be smaller than that in SmA phase. This situation is called layer shrinkage.

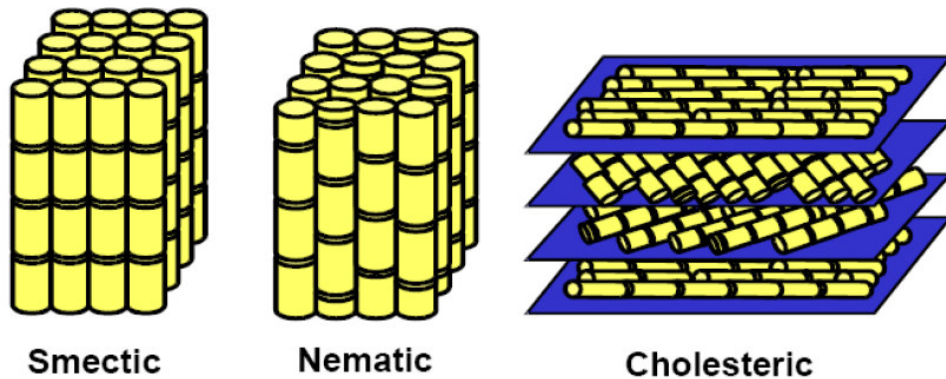


**Fig 1.1** Molecular arrangements structure of liquid crystal phases.

### **Chiral smectic C**

When chiral dopants are mixed with achiral molecules in smectic C phase, the Ferroelectric chiral smectic C phase ( $\text{SmC}^*$ ) is formed. When the molecules of mixture become chiral, successive smectic C layer shows a gradual change in the direction of tilt, so that the director precesses about the z-axis from layer to layer, as illustrated in Fig.1.2.

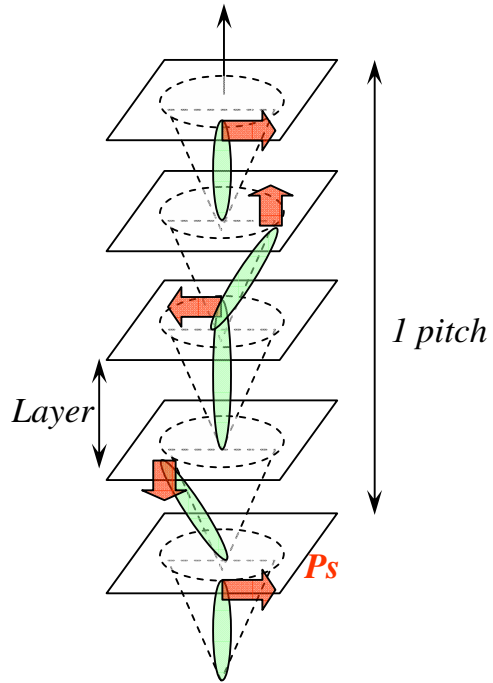


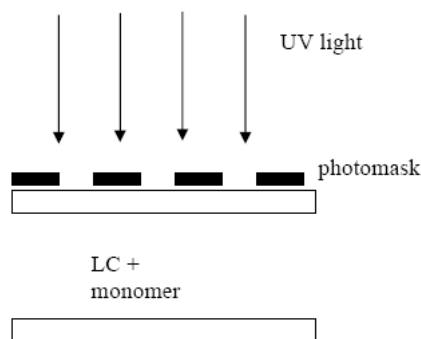
**Fig 1.2** The helix in a layer structure of the SmC\* liquid crystal.

In addition to bring about the helical structure, chirality would also induce a spontaneous polarization ( $P_s$ ), shown by the red arrows in Fig.1.2. This polarization vector is perpendicular to the director and locating on the plane of layer. In bulk SmC\* material, freely developing helical structure, ferroelectricity does not show up since the polarization of all directions will average to zero over one pitch, resulting in no macroscopic polarization in the system. Application of electric field, of which the direction is normal to helical axis, would accompanies the polarization vector toward the field direction and unwind the helix. Thus, the  $P_s$  could be oriented in the direction of external field. Furthermore, Clark and Lagerwall [9] presented the so-called surface-stabilized ferroelectric liquid crystal (SS-FLC) which suppressed the helix by placing the SmC\* material inside a very thin cell, and this insight opened a new area for display application.

## 1.3 Types of Liquid Crystal Gratings

### 1.3.1 Liquid Crystal Phase Grating Review

Recently, it has been reported that several methods develop liquid-crystal gratings. Among these methods, it is always expected that the performance of LC gratings can be achieved a high level until now, so new methods or advanced methods have been proposed abidingly. In Fig 1.3 (a), One approach is to use a photomask [10]. The cell filled with a mixture is illuminated with ultraviolet light (UV) through the photo-mask with a pattern. In the illuminated areas monomer crosslinking occurs creating polymer rich regions, and LC is expelled into dark regions. Another approach to create varying light distribution in the sample is to use interfering coherent optical beams as show in Fig 1.3 (b). From Equation (1.1), the patterned period can be controlled by the wavelength and an incident angle of two coherent beams [11]. The second approach has the advantage of higher resolution and the possibility to create a slanted grating. However, in the first approach the resolution is limited not only by the photomask, but also by the diffraction effects of UV light. Furthermore, the third approach is to use patterned electrodes. In Fig 1.3 (c), the device with a unity mark-space metal stripe is assembled and injected pure phase grating, so it can reach high efficiencies [12].



(a)

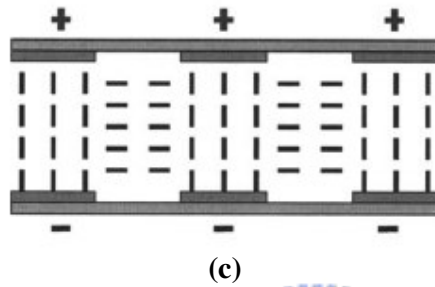
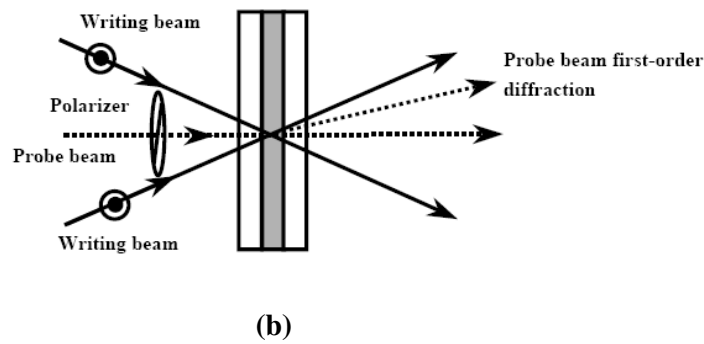
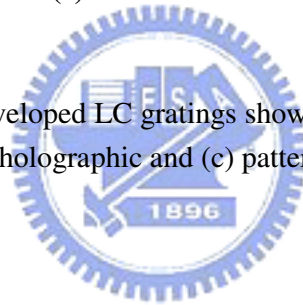


**Fig 1.3** Three types of developed LC gratings show: (a) patterned photo-polymerization (b) holographic and (c) patterned electrodes.



### 1.3.2 Laser-Induce Holographic Gratings

Photo-induced reorientation effects in dye-doped liquid crystals (DDLCs) have recently attracted significant attention. Janossy et al. found that photo-excited anthraquinone dye molecules induced a positive torque, facilitating the reduction of the threshold of the optical Freedericksz transition [13]. Gibbons et al. demonstrated that nematic liquid crystals (NLCs) were reoriented perpendicularly to the optical electric field, when the substrate, coated with an azo-dye doped polyimide, was excited by linearly polarized light [14]. It is no doubt that holographic alignment technique has advantages of higher resolution and the possibility to create a slanted grating [15-17].

According to the reference [18], Fig 1.4 show a polarization interference pattern created from the interference of right-handed (RH) and left-handed (LH) circularly polarized light. In the reference, an azo-dye-doped liquid crystals is used and azo-dye molecules can reorient depending on the local polarization of light via photoactivated isomerization. When exposed to light, the excess absorbed energy translates in a conformational change from a trans-longitudinal to an unstable cis-excited state. The absorbed energy in the trans states is proportional to the orientation of the molecular axis with respect to the local polarization due to the anisotropic nature of azo-dye. Such an angular dependence will tend to slowly align the dye molecules in the minimal-energy configuration, which is perpendicular to the local polarization. Therefore, different polarization states can induce LC molecules orientation. Such a pure phase grating is fabricated by this way.

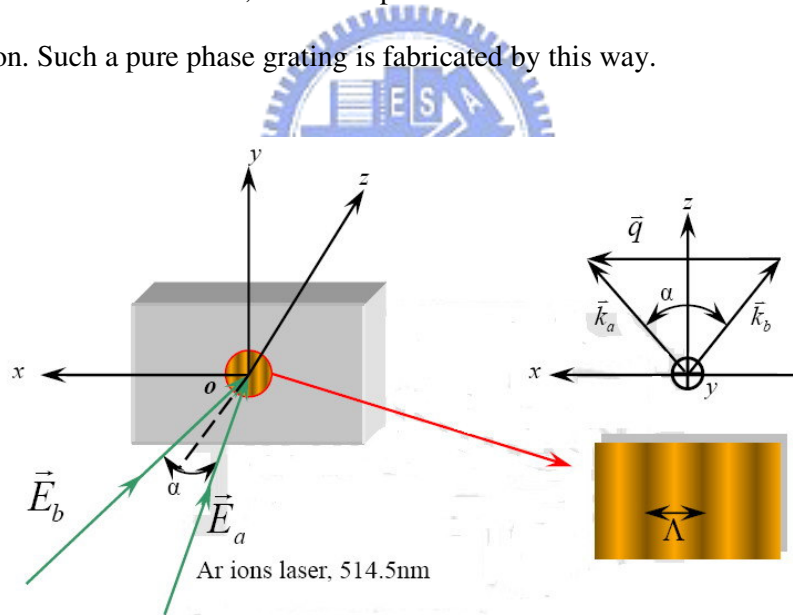


**Fig 1.4** Schematic illustration of the polarization interference pattern.



### 1.3.3 Patterned Photo-polymerization

Spatially periodic patterning of the anchoring condition of a nematic liquid crystal (NLC) within a polymer matrix via a patterned photopolymerization affords a novel and facile method to prepare electrically switchable diffraction gratings [19-20]. UV irradiation through a photomask of two comonomers, with opposite tendencies to align the NLC and also with different reactivity ratios, leads to definition of areas with either homeotropic or planar alignment of the NLC. Photopolymerization-induced diffusion of the monomers accounts for the spatial distribution of the concentration of these monomers. The resulting diffraction gratings are switchable under low electric fields and possess structural stability offered by the polymer matrix. From Fig 1.5, initially, the grating texture has grating effect due to two effective refractive indices of two alternating domains without applied voltage. At the applied voltage, all LC molecules has been rotated homeotropically, so the texture should show one domain but has slight grating effect because the index of polymers mismatch the index of liquid crystal.

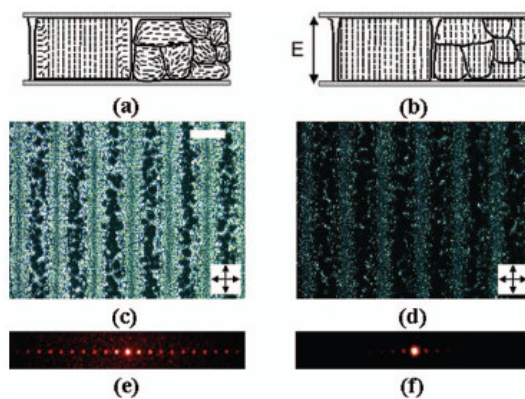


**Fig 1.5** (a) and (b) Schematic of the side view of the LC-polymer film with two alternate stripes of different anchoring and morphology. (c) and (d) Light micrographs of the LC-polymer grating film between crossed polarizers. (e) and (f) Diffraction patterns of the same film with a normally incident 633 nm He-Ne laser.

### 1.3.4 Patterned-ITO Electrodes

The conventional device with a unity mark-space metal stripe is applied for LC beam splitters or LC blazed grating beam deflector in several years [21] [22]. Fig 1.6 (a) shows the structure consists of two ITO glasses with one patterned stripes and liquid crystals sandwiched between two ITO glasses. The electric field is a symmetric curvature as show in Fig 1.6 (b). LC molecules are rotated along the electric field. We can operate one domain alignment in strong electric field alignment with applied voltage but the fringing field still affects the another domain alignment. As a result, the phase profile is smooth or sinusoidal but not square. The fringing field plays an important role for the performance of this structure, so some parameter such as thickness of the cell, the unit mask period, and optical properties of liquid crystals are considered.

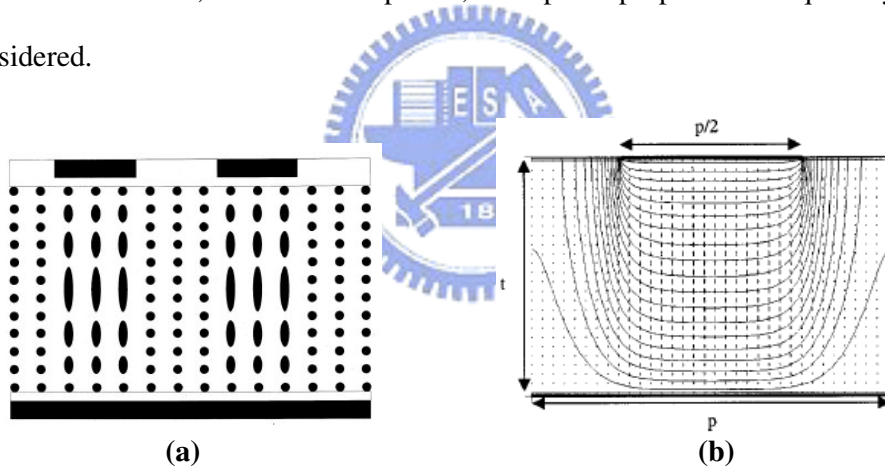


**Fig 1.6** (a) the structure with a unit pattern glass (b) the director profile for anti-parallel alignment.

## 1.4 Projection Displays by Binary Phase LC Gratings

The device consists of two alternating stripes by double-rubbing technique [23]. Each stripe is a hybrid liquid crystal cell with adjacent stripes oriented perpendicularly as show in Fig 1.7. It is found that x-component polarization or y-component polarization both correspond to the phase difference  $(n_{eff} - n_o)$  that means diffraction efficiencies are identical. In the case of  $\Delta\phi = \pi$ , polarizations will be diffracted in the first order and vanish in the zero order. Polarizations remain the zero order without applied voltage. By this way, we can control polarizations to pass or not pass the output louvers as show in Fig 1.8. This kind of electro-optically controlled diffraction grating in principle gives 100% diffraction efficiency and no polarization direction dependence

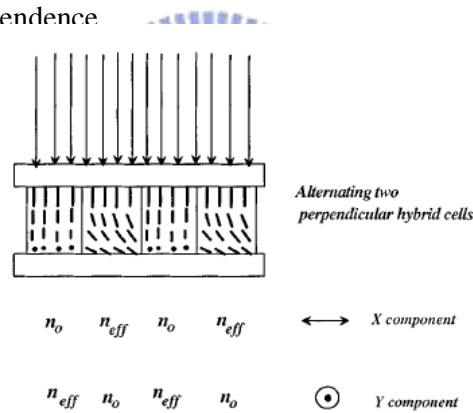


**Fig 1.7** A hybrid liquid crystal cell with adjacent stripes oriented perpendicularly.

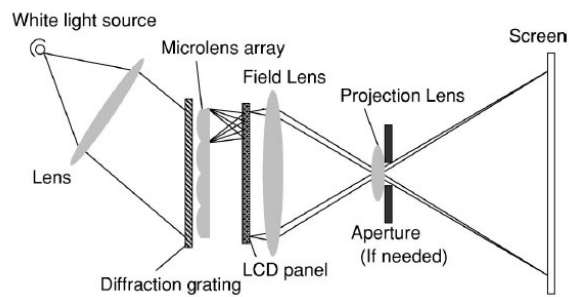


**Fig 1.8** Optical setup of the multi-primary display for the LCD projection system.

## Chapter2

# Ferroelectric Liquid Crystal Phase Grating

### 2.1 Introduction of FLC Phase Grating

Recently, various ferroelectric liquid crystal phase gratings have been developed and expected to be applied in the applications of optical communication and projection displays. However, unresolved issues, such as complicated fabrication, low diffraction efficiency, low contrast ratio and high fringing field effect, still remained. In this study, a simple phase grating fabrication method using ITO (indium tin oxide) etched pattern was proposed. Fig 2.1 shows the structure. LC molecules were reoriented by electric field in the patterned ITO area, while LC molecules remain aligned with rubbing direction in the area without ITO. Thus, the binary phase gratings were formed periodically between alternating domains.

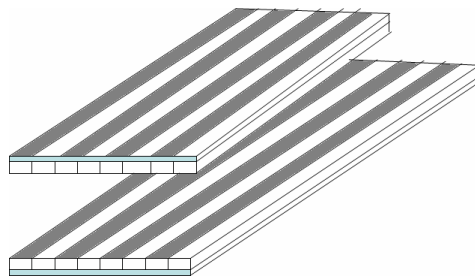


**Fig 2.1** The structure of our designed-cell

Ferroelectric liquid crystals were proposed to solve the slow response time of nematic liquid crystal devices in previous study [24-26]. However, the alignment defects and high driving voltage induced fringing field effect reduced the diffraction efficiency. To improve the alignment of SSFLC device, DC voltage was usually applied during annealing [27]. However, this method is not workable in ITO-patterned grating device in the area without ITO. Thus, an asymmetric hybrid cell was utilized to suppress alignment defects [28-30]. Avoiding the fringing field effect, several methods were proposed, such as low driving voltage materials used, increasing the cell gap and increasing the period of the patterned-ITO. Thus, a desirable fast switching, low driving voltage, high diffraction efficiency and easy process FLC grating was presented.



## **2.2 Overview of SSFLC Devices**

### **2.2.1 SSFLC Structure**

In 1980 Clark and Lagerwall [31] proposed a new device structure which can unwind the helix of a SmC\* material if the cell gap between two plates was much smaller than the helical pitch ( $\ll 1$  pitch), as shown in Fig 2.2. In addition to having sub-microsecond switching, two symmetric stable states existed so that the device was bistable. The spontaneous polarization vector,  $P_s$  was tangential to the molecule and perpendicular to the alignment surface. Molecules of two stable states aligned in different direction accompanying with upward and downward  $P_s$ , respectively. We called this as surface stabilized ferroelectric liquid crystals (SSFLC).

Besides, the LC molecules motion under applied electric field was similar to in-plane-switching mode (IPS mode) so that SSFLCs had wide viewing angle merit. Fast response time and wide viewing angle characteristics were suitable for field

sequential displays, which attracted many researchers. Although SSFLC had superior advantages in field sequential displays, its inherent poor alignment causes serious light leakage and hindered the commercialization development. In this section, the reasons and theories of poor alignment would be reviewed. Also solving method would be proposed from theories.

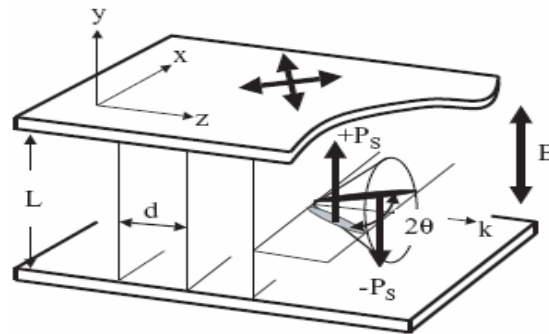


**Fig 2.2** The construction and operation of the SSFLC cell.

### 2.2.2 Zigzag Defect in SSFLC

The resulting chevron structure founded by Rieker [32] et al. in 1987 with X-ray scattering method is one of the major obstacles for the application of SSFLC. The most severe problem resulting from chevron structure is the zigzag defect.

Zigzag defects formed when domains with chevrons pointing in opposite directions interspersed as shown in Fig 2.3 (a). Both the top and bottom substrates are treated identically and the rubbing directions of the two alignment films are parallel. C1 is the structure of which the chevron kink is opposite to the rubbing direction; C2 is the structure of which the chevron kink is parallel to the rubbing direction. Zigzag usually shows up with hairpin defect and lightning defect as illustrated in the bottom of Fig 2.3 (b). A thick wall hairpin defect is generated in the location where the apexes of C1 and C2 meet. Thin lines of lightning defect are produced where the apex of C1

is far away from the apex of C2. The hairpin defect usually grows along the smectic layer; however the lightning lines are running parallel to the rubbing direction. Zigzag defect severely degrades display device because light leakage occurs at the edge of the zigzags which results in low contrast.

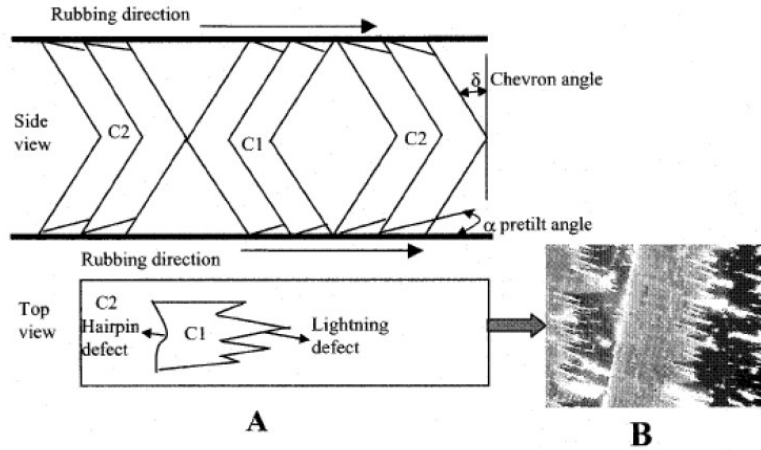


**Fig 2.3** (a) The upper figure shows the chevron structure of C1 and C2 states, and the lower one shows the shape of zigzag. (b) Picture of zigzag defect under POM.

### 2.2.3 Horizontal Defect in SSFLC

In common LCD production, the rubbing process was often adopted to align the liquid crystal molecules so that the LC molecules would fix at the surface of alignment layer and force the bulk LC to orient toward rubbing direction. In SSFLC, molecules would also align along the rubbing direction but lie on two different cones so that a folding of smectic layer took place, as shown in Fig 2.4. Multi-domains were forming with spontaneous polarization pointing upward or downward into the substrate. The reason why two kinds of directors were generated was explained as following. When the cell entered the SmC\* phase, two directions of smectic layers were formed and tilted respect to the rubbing direction.

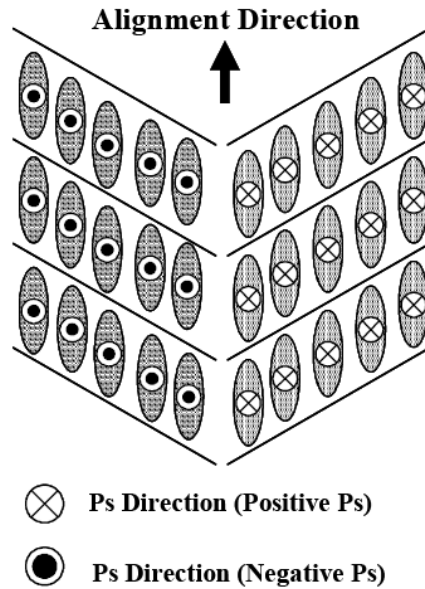


**Fig 2.4** Schematic illustration of the horizontal chevron domain structure, as a top view in the surface stabilized state with unwound helix.

When an electric field was applied to the cell with multi-domain, the adjacent domains switched in different ways [33], as shown in Fig 2.5. The type A domain only responding to a positive field turned to the bright state when a positive voltage was applied. On the other hand, when a negative voltage was applied, only the type B domain switched to bright. Multi-domains resulted in light leakage and reduced the contrast ratio.

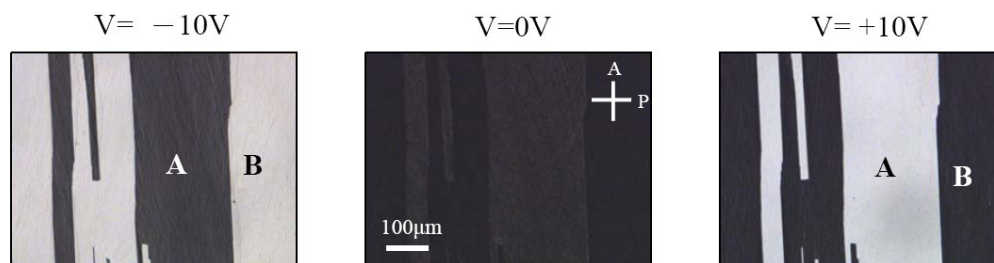


**Fig 2.5** Microscopic pictures of multi-domain cell and its response to electric field.



### 2.2.4 Methods to Erase Zigzag Defect

There were three methods to get no zigzag defect cells. The first two methods were to get C1 or C2 uniform orientation only within one cell. Kanbe et al. reported that a combination of the high pretilt aligning film and a low tilt angle for the FLC material was required to obtain the C1U state and prevented the appearance of the C2 state. In the application of display, Kodan et al [34]. and Tsuboyama et al [35]. showed good display performance with a uniform C1U orientation by using a high pretilt alignment layer with a low tilt FLC material.

About C2 uniform orientation, two useful approaches to realize the formation of a C2U orientation had been reported. One approach involved an investigation of the method of alignment. The C2 orientation was possible in the low pretilt angle condition, but it was impossible in the high pretilt angle condition. Strong rubbing had also been reported as being favorable to producing the C2 orientation because the direction of molecules on a surface in the C2 orientation because almost the same as the direction of rubbing and that was insensitive to variations in alignment, surface polarity, memory effects and surface switching. The other approach was to investigate the relationship between the properties of materials and the formation of C2 orientation. To obtain the C2 orientation, a material must be in the SmA phase over a wide range of temperatures. This was because the FLC materials were in SmA phase over a wide range of temperature tended to have small tilt angles near the SmC to SmA transition point. This small tilt angle could reduce the energy barrier for transition from the C1 to the C2 state near the SmC to SmA transition point because the small tilt angle led to chevron layers leaning at a small angle. Besides, Furue et al. adopted polymer-stabilized method to obtain free C2U orientation.

The last approach to get zigzag defect was quasi-bookshelf structure. Three major approaches had been investigated to obtain a bookshelf layer structure. First approach was AC-field treatment [36]. An initial chevron layer structure is turned into a bookshelf layer structure by applying a strong low frequency AC field. High  $P_s$  of FLC material was required because the interaction between the electric field and  $P_s$  induces a torque that changed the layer structure from chevron to bookshelf.

Second approach was utilizing a unique class of materials with tilt angles that were weakly dependent on temperature. In the previous section, the chevron layer structure was the reduction of layer spacing brought about by cooling. The reduction of layer spacing was usually observed in FLC materials with an INAC (Iso-N-A-C) phase sequence; because the tilt angles of such FLC materials were usually strongly dependent on temperatures. However, there was unique of FLC materials with an INC (Iso-N-C) phase sequence which the tilt angles were weakly dependent on temperature [37]. It was possible to realize a bookshelf layer structure without electrical field.

Third approach utilized FLC materials with an INC phase sequence, the DC voltage applied during the material cooled and changed from the N to SmC phase. The quasi-bookshelf orientation was suitable for active matrix drive method, because it exhibited mono-stable and a smooth V-T characteristic. This mode was called CDR (continuous director rotation) or Half-V shaped FLC [38-39].

### 2.2.5 Eliminate Horizontal Defect

The polarity of the alignment layer surface has much influence on alignment phenomena for FLC material, the sign of the polarity is defined as negative when the dipole on the surface is directed toward from the surface to the liquid crystalline material for the positive FLC materials as shown in Fig 2.6 [40]. The sign of the polarity on the alignment layer can be determined by using the dissymmetric cell with the two different alignment layers by Dijon [41], the other method of determining the alignment layer polarity by Takatoh et al [42].

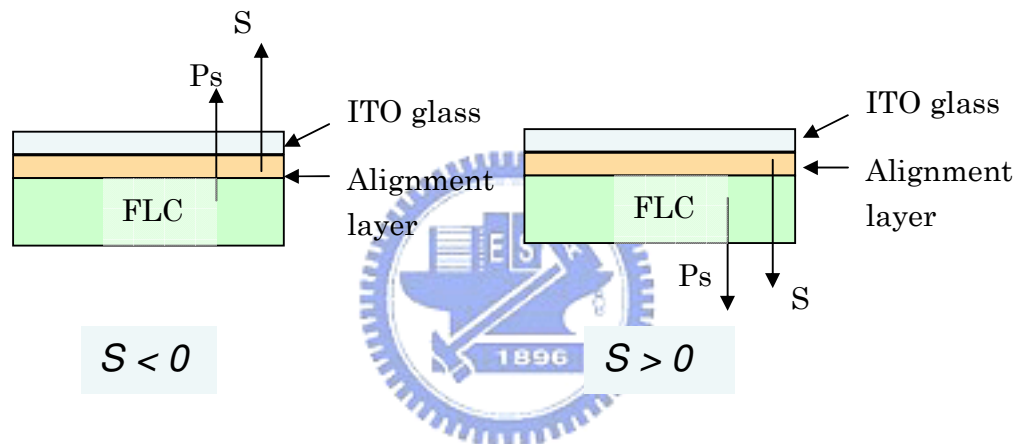


**Fig 2.6** Sign of surface polarity and the direction of the dipole moment.

The horizontal chevron defect with two different layers usually occurs in a symmetric structure cell with the same alignment layer and rubbing strength on both ITO glass. In order to solve this problem, an asymmetric cell with two different polarity of alignment layer (PVA and PI) is used in our study. This cell structure is called as hybrid cell, and the hybrid cell is expected to generate the below model as shown in Fig 2.7. Because the PI can induce the upper direction of  $P_s$  to direct outward of the surface and vice versa in bottom plate, one smectic layer maybe formed in the parallel rubbing.

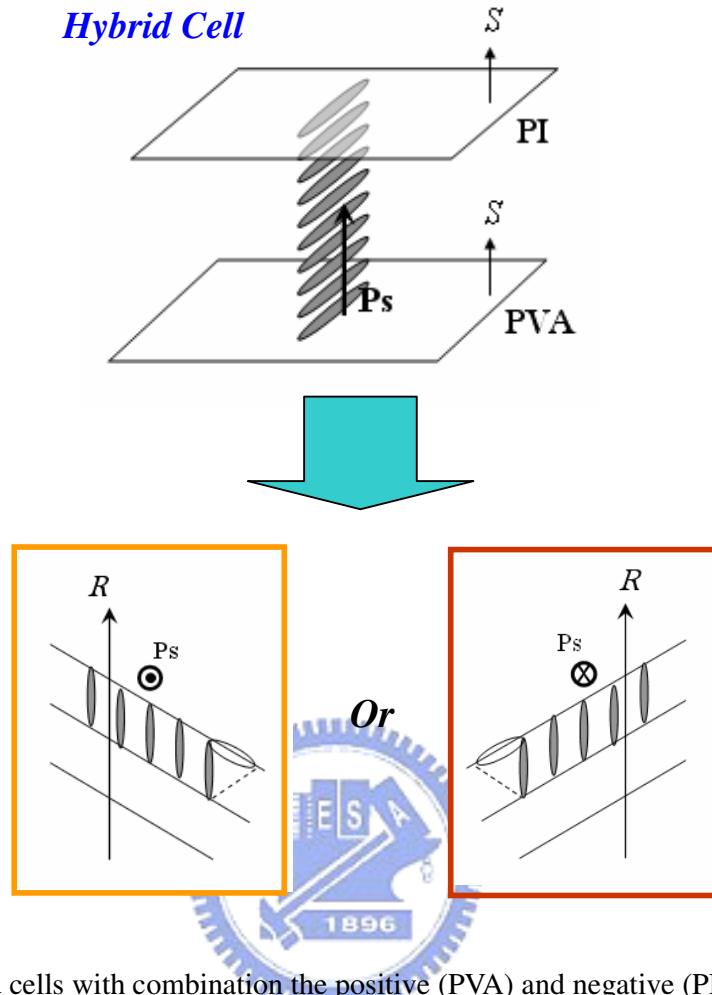


**Fig 2.7** Hybrid cells with combination the positive (PVA) and negative (PI) alignment layers.

### 2.2.6 Summary

Molecular orientation is a very important factor in determining the performance of a device in the development of practical FLC phase grating. In previous description realizes the molecule orientation state and the causes of zigzag and horizontal defect. Next, we discuss how to eliminate defects and stabilize in uniform state related to the SSFLC phase grating device.

### 2.3 The Basic Theory of Polarizing Binary Diffraction Grating

A polarizing beam splitter that uses binary phase gratings written onto a liquid-crystal spatial light modulator is reported according to the reference [43-44]. These gratings produce several linearly polarized diffracted orders and a zeroth-order beam whose polarization state can be completely controlled. The basic theory of binary phase polarization gratings is shown.

The Jones matrix  $G(h, v)$  representing a grating  $t(x)$  encoded onto the liquid-crystal spatial light modulator (LCSLM) can be written as

$$G(h, v) = \begin{pmatrix} 1 & 0 \\ 0 & t(x) \end{pmatrix} \quad (2.1)$$

Here,  $h$  and  $v$  refer to the horizontal and vertical polarization states, respectively.

Binary phase diffraction grating function  $t(x)$  varies as a function of position along the LCSLM, as shown in Fig 2.8. Each period  $d$  of the grating is separated into a region with width  $w$  and phase shift  $\phi_1$  and a second region with width  $d - w$  and corresponding phase shift  $\phi_2$ .

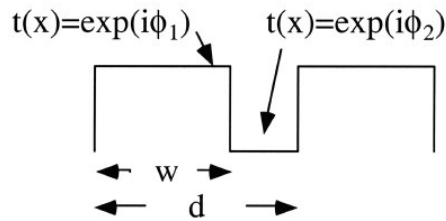


**Fig 2.8** Diffraction grating showing a period of the grating with two areas with different widths and phase shifts.

Transmission function  $t(x)$  can be decomposed into a Fourier series as

$$t(x) = \sum_{n=-\infty}^{\infty} c_n \exp(in2\pi x / d) \quad (2.2)$$

$$c_n = \frac{1}{d} \int_0^d t(x) \exp(-in2\pi x / d) dx \quad (2.3)$$

Note that at the dc term (when  $n= 0$ ) is not diffracted, whereas all other terms are diffracted into angles that are proportional to the values of  $n$ . Consequently, our Jones matrix function can be divided into two parts as

$$G(h, v) = \begin{pmatrix} 1 & 0 \\ 0 & t(x) \end{pmatrix} = \begin{pmatrix} 1 & 0 \\ 0 & c_0 \end{pmatrix} + \begin{pmatrix} 0 & 0 \\ 0 & \sum_{n \neq 0} c_n \exp(in2\pi x / d) \end{pmatrix} \quad (2.4)$$

We can control the parameters and make a number of simplifying conditions. First, if the difference between the two phase is  $\Delta\phi = \phi_2 - \phi_1 = \pm\pi$ , and the coefficients in Eq.2.3 simplify to

$$c_0 = \exp(i\phi_1) \left( \frac{2w-d}{d} \right)$$

$$c_{n \neq 0} = \frac{2 \exp(i\phi_1) \exp(in\pi w / d)}{\pi n} \sin\left(\frac{n\pi w}{d}\right) \quad (2.5)$$

We input a linear polarization with the grating at the angle

$$E = \begin{bmatrix} \cos(\alpha) \\ \sin(\alpha) \end{bmatrix} \quad (2.6)$$

As a result, the output electric field vector can be written as

$$\begin{bmatrix} E_H \\ E_V \end{bmatrix} = \begin{bmatrix} \cos(\alpha) \\ c_0 \sin(\alpha) \end{bmatrix} + \sum_{n \neq 0} \exp\left(\frac{in2\pi x}{d}\right) \begin{bmatrix} 0 \\ c_n \sin(\alpha) \end{bmatrix} \quad (2.7)$$

For the device, we design that the horizontal polarization state is not affected by the LCSLM but a vertical polarization is diffracted in high order terms. their strengths are proportional to the ratio  $w/d$  as well as the angle  $\alpha$  of the input polarization state.

Figure 2.9 shows the transmission of the diffraction pattern through a linear polarizer with different orientations for the case in which  $\phi_1 = 2\pi$  and  $\phi_2 = \pi$ . Figs. 2.9 (a) and 2.9 (c) show that the zero order is linearly polarized at an angle of  $+45^\circ$  and Figs. 2.9 (b) and 2.9 (d) show that the first orders are polarized at  $90^\circ$ .

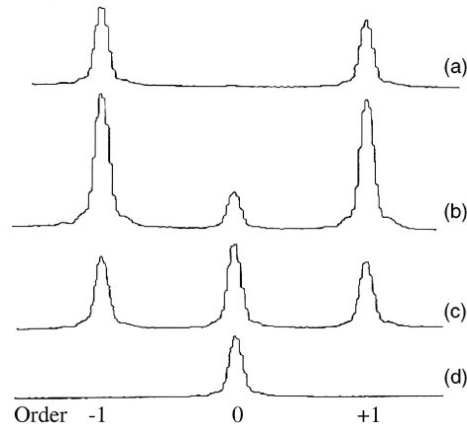


**Fig 2.9** A grating with a linearly polarized zero order at  $+45^\circ$ .  
The analyzer polarizer is oriented as (a)  $-45^\circ$  (b) horizontal  
(c)  $+45^\circ$  and (d) vertical.

The diffraction efficiency is defined as equation

$$\eta_k = \frac{I_k}{I_i} \quad (2.8)$$

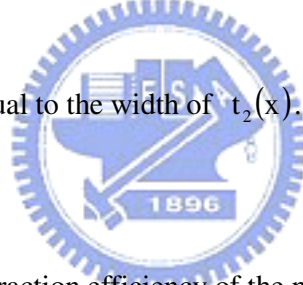
Where  $\eta_0$  is the diffraction efficiency of k-order,  $I_k$  is the intensity of k-order and  $I_i$  is the initial intensity of non-diffracting laser beam.

For  $\Delta\phi = \phi_2 - \phi_1 = \pm\pi$ , the diffraction efficiency of the nth order is given by

$$\eta_{n=0} = \left(\frac{2w-d}{d}\right)^2 \quad (2.9)$$

$$\eta_{n \neq 0} = \left[\left(\frac{2}{\pi n}\right) \sin\left(\frac{n\pi w}{d}\right)\right]^2$$

For the width of  $t_1(x)$  is equal to the width of  $t_2(x)$ .



From equation, the diffraction efficiency of the nth order is given by

$$\eta_k = \left\{ \begin{array}{l} \cos^2(\Delta\phi/2) \\ \left[\left(\frac{2}{k\pi}\right) \sin(k\pi/2)\right]^2 \sin^2(\Delta\phi/2) \end{array} \right\} \quad (2.10)$$

$$\Delta\phi = \phi_1 - \phi_2 = \frac{2\pi t(n_{eff} - n_o)}{\lambda} \quad (2.11)$$

Where  $\Delta\phi$  is the relative phase difference between two adjacent two regions in the binary grating system.



For  $\Delta\phi = (2n + 1)\pi$  ( $n = \text{integer}$ ), the diffraction efficiencies of odd orders ( $k = \pm 1, \pm 3, \pm 5, \dots$ ) have the maxima while the zero order or the non-diffracted beam has the minima of zero. For the case that  $\Delta\phi = (2n + 1)\pi$ , the diffraction efficiencies of odd orders ( $k = \pm 2, \pm 4, \pm 6, \dots$ ) have the minimal value. In the case of  $\Delta\phi = \pi$  The diffraction efficiency of the zero order is  $\eta_0 = 0\%$ . The diffraction efficiency of the first order is  $\eta_{\pm 1} = 40.5\%$ . The diffraction efficiency of the first order is  $\eta_{\pm 3} = 4.5\%$ .

## 2.4 Optical Properties of Liquid Crystals

The refractive indices of anisotropic materials are conveniently represented in terms of the optical indicatrix, the surface of which maps the refractive indices of propagating waves as a function of angle. Solution of Maxwell equation for an anisotropic medium leads to the result that for a particular wave-normal, two waves may propagate with orthogonal polarization and refractive indices. An ellipsoid having as semi-axes the three principal refractive indices define the optical indicatrix. In general for any wave-normal, the section of the indicatrix perpendicular to the wave-normal direction will be an ellipse, and the semi-axes of this ellipse are the refractive indices of the two propagation waves. Figure 2.10 shows the index ellipsoid.

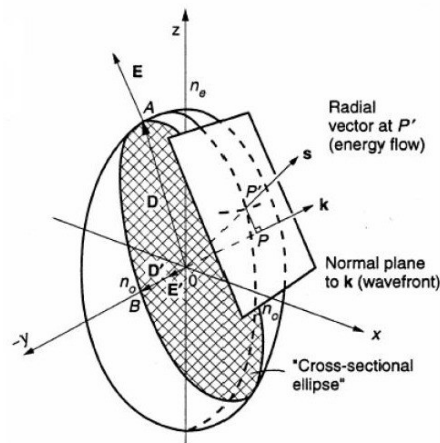


**Figure 2.10** Normal modes determined from the index ellipsoid.

The overall phase symmetry of an anisotropic material will determine the number of independent refractive indices. A cubic or isotropic phase has only one refractive index, which is independent of direction, so the corresponding indicatrix is sphere, and only ray will propagate in any direction. Phase with a greater than two-fold symmetry axis have only two principal refractive indices, so the corresponding indicatrix is an ellipsoid of revolution. Thus for ray traveling along the symmetry axis, the perpendicular section is circular, and the corresponding refractive index is called the ordinary refractive index  $n_o$ . When viewed along this special direction, known as the optic axis, any material behaves optically like an isotropic material. Such materials are known as uniaxial, since there is a single optic axis. For wave-normal is perpendicular to the optic axis, then one refractive index is  $n_o$ , and the other corresponds to the semi-axis along the symmetry axis, and is called the extraordinary refractive index  $n_e$ . In general for wave-normal at some arbitrary direction making an angle of  $\theta$  to the optic axis, two waves can propagate; one is always an ordinary ray, refractive index  $n_o$ , while the other propagates with an effective refractive index given by:

$$n_{\text{eff}} = \frac{n_o n_e}{(n_e^2 \sin^2 \theta + n_o^2 \cos^2 \theta)^{1/2}} \quad (2.12)$$

All low molecular weight thermotropic liquid crystal so far characterized are uniaxial, so they have just two principal refractive indices,  $n_e$  and  $n_o$ , and the difference between these the birefringence  $\Delta n = (n_e - n_o)$ . The optic axis is coincident with the director, and the principal refractive indices are often denoted as  $\tilde{n}_{\parallel} \equiv n_e$  (parallel to the director), and  $\tilde{n}_{\perp} \equiv n_o$  (perpendicular to the director)

## 2.5 Analysis of FLC Phase Grating

### 2.5.1 Grating Schematic

In recent years, FLC materials are advanced and popular materials due to characteristic of the fast response time and bistable capability. According to the reference [45], the FLC grating structure is shown in Fig 2.11. The optic axis is tilted by  $\theta_u$  from the x-axis in the up region and tilted by  $\theta_d$  in the down region. It is assumed that the stripe length for the y-axis is infinite and that the grating is thin. The up-region stripe width is “a” and stripe pitch is “b”. A polarizer is fixed to the x-axis. The incident beam is linearly the grating. After fabricating the grating, alternating stripes consist of photo-polymerized regions (Down regions) and nonphoto-polymerized switchable regions (Up regions) are formed. FLC molecules align along the same direction without applied voltage, so grating effect is not obvious. Under an electric field, FLC molecules are reoriented due to  $n_o$  director along the electric field and produce phase grating. Thus tunable FLC phase-grating devices are easily formed.

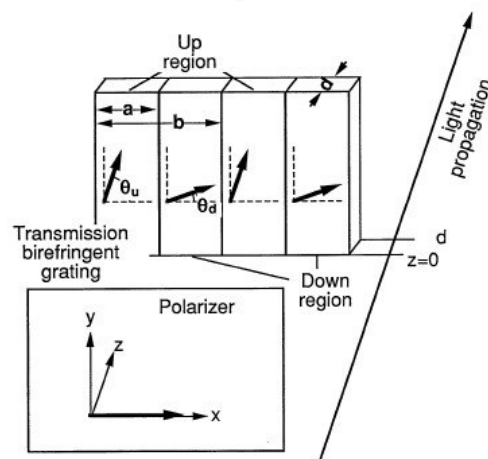


**Fig 2.11** Optical setup of a grating and dimensions.

### 2.5.2 Diffraction Model

Electric fields of the beams are represented by  $E_x$  and  $E_y$  that correspond to the components parallel to the x- and y-axes, respectively. A horizontally polarized beam,

$$E_x = \exp(-j\omega t), \quad E_y = 0 \quad (2.13)$$

is incident on the grating, where the amplitude of the field  $E_x$  is assumed to be unity. The x- and y-components of the fields represent p- and s-polarizations, respectively. Just after passing the down region of the birefringent grating ( $z = d$ ), the light fields become

$$E_d^e = \cos \theta \cdot \exp\{j(\delta_e - \omega t)\} \quad (2.14)$$

for the extraordinary beam and

$$E_d^o = -\sin \theta \cdot \exp\{j(\delta_o - \omega t)\} \quad (2.15)$$

for the ordinary beam. The phase shifts here are  $\delta_e = kdn_e$ ,  $\delta_o = kdn_o$  and  $k = 2\pi/\lambda$ ;  $d$  is the grating cell thickness, and  $n_e$  and  $n_o$  are the refractive indexes for the extraordinary and ordinary beams, respectively.

### 2.5.3 Polarization-independent FLC Phase Grating

According to related references [46], a polarization-independent FLC phase grating has been successfully prepared. Fig 2.12 shows grating textures applied with different voltages. As a result of two periodically alternating domains, the incidence of light along z axis, polarized along the rubbing direction (x axis), the refractive indices are ordinary ( $n_o$ ) and extraordinary ( $n_e$ ) in the photo-polymerized and fully switched non-polymerized regions, respectively. For the incidence of y-polarized light,

$n_o$  and  $n_e$  are interchanged. When light passes through each region, the phase difference arises between these two regions by  $2\pi d(n_e - n_o)/\lambda$ , where  $d$  and  $\lambda$ , respectively, are the cell thickness and the wavelength.

Then the diffraction occurs. The difference in the refractive indices (birefringence)  $\Delta n$  is  $n_e - n_o$  for both x-polarized and y-polarized light, so that the diffraction efficiency does not depend on the polarization. Even for incident polarizations with arbitrary angles to x and y axes, the situation is the same for the components parallel to x and y axes, if molecules would switch in the x-y plane. Then, polarization-independent phase grating is realized.

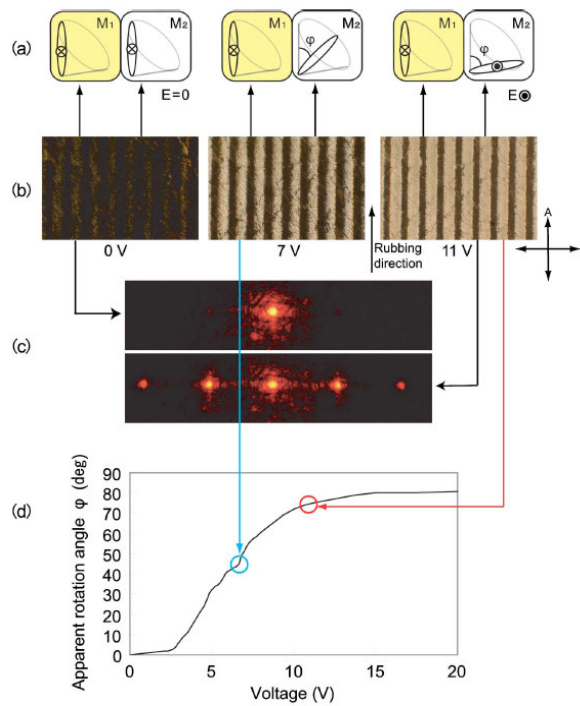


**Fig 2.12** The principle of the polarization-independent FLC phase grating.

## Chapter3

### Materials 、 Fabrication Process and Instruments

#### 3.1 Introduction of Grating Pattern Process

This chapter will describe fabrication process and instruments in study. Two kinds of ITO-thickness glasses were prepared for this study. In order to avoid an additional phase, glasses with thin-thickness ITO prepared were required. Therefore, ITO-coated glass plates of 12nm thickness were used. In addition, grating masks were designed first by AUTO-CAD software. In fabrication process, photolithographic techniques were important and complicated. However, this problem has been solved and parameters of the etching were tested and used. In the case of liquid crystal materials R3206\_50 and hybrid alignment SSFLC cell were prepared. Furthermore, instruments such as polarizing optical microscopy (POM), atomic force microscopy (AFM), cell gap measurement system and laser optical systems were all applied to measure grating textures, the thickness of ITO, cell gap and diffraction efficiencies respectively.

### 3.2 Grating Pattern Mask Design

The software of AUTO-CAD was used and the periods of patterned ITO stripe were designed of 20um-20um, 40um-40um and 38um-42um. The dimension of the glass plate was 3cm×3cm and included the region of the designed-grating pattern which is 2cm×2.5cm. The Fig 3.1 shows the designed-patterns of masks.

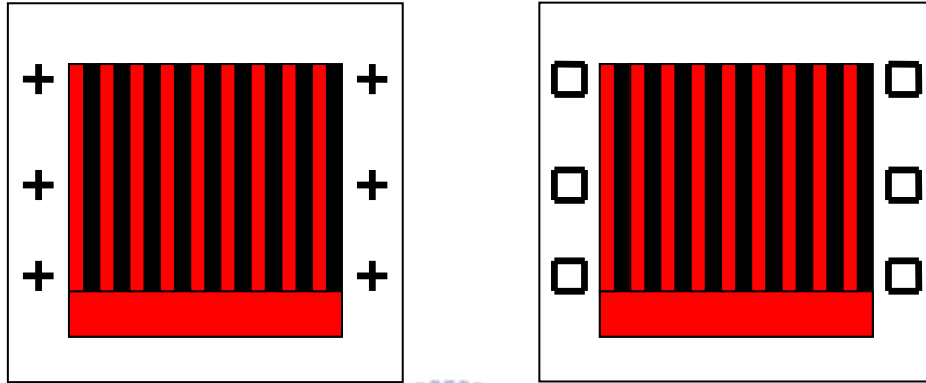


**Fig 3.1** The black and white color regions both represent non-ITO patterns and the red color regions represent etched-ITO patterns.

In designing process, some essentials should be paid attention to. For example, when the two plates with designed-pattern have been finished, they should be observed and overlapped by POM (Polarizing Optical Microscopy). In order to overlap the two plates accurately, alignment marks must be designed in the pattern of the mask and observed by reflective mode of POM due to thin-thickness ITO glasses. In Fig 3.1, alignment marks were showed.

### 3.3 Fabrication Process

Two fabrication processes include to mix materials and to make hybrid cell. To prepare R3206 and R3206H, R3206 mixtures were made by mixing R3206H, the R3206H has the same phase sequential temperature as R3206 without chirality. On the made hybrid cell, 50%wt. PI and 2.5%wt. PVA were prepared in fabrication process, the PI and PVA have different polarity as alignment layer. The detail steps of two fabrication processes will describe in following sections.

#### 3.3.1 Materials Preparation

Step1: On the electronic scale, the desirable weight of R3206 and R3206H were put together in a 20ml vial.

Step2: The mixture were dissolved by using glass rod to stir it on the hot-plate at 120°C.

#### 3.3.2 Cell Fabrication Process

The major of process is presented as shown in Fig 3.2.

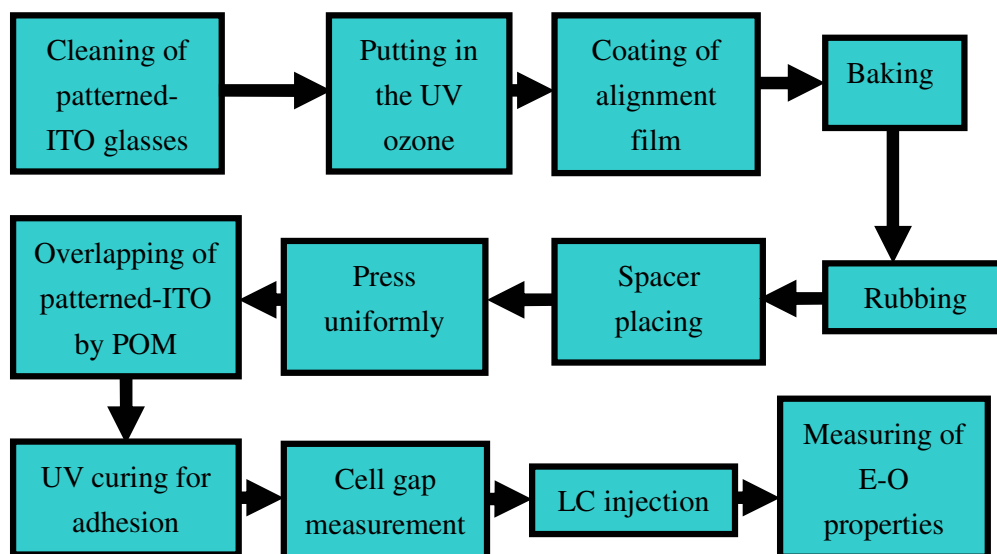




**Fig 3.2** The flow chart of cell fabrication process.

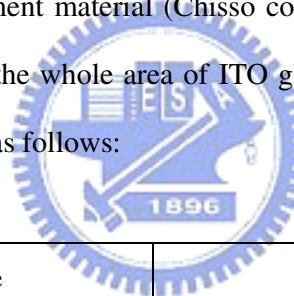
Step1: The patterned-ITO glass was washed by using detergent.

Step2: The ITO glass was vibrated for 30 minutes by using supersonic oscillator.

Step3: On the ITO glass, the water of surface was blow off with nitrogen gas firearm, then put it on hot-plate and bake it for 30 minutes at 110°C.

Step4: The UV-ozone treated surface of ITO glass for 20 minutes that is for better adhesion of alignment layer.

Step5: Put the ITO glass on the spin coater. To drop the solvent of alignment material (Chisso company NB-32 for polyimide, DI-water for PVA) onto the whole area of ITO glass, next wait 30 seconds, then spin. After spin-coating, to drop the solution of alignment material (Chisso company PIA-X660-01X, Aldrich company PVA) onto the whole area of ITO glass, next wait 30 seconds, then spin. The spin rate is as follows:



50%wt. Polyimide			2.5%wt. PVA		
	Rate	Time		Rate	Time
1st	800rpm	30sec	1st	500rpm	30sec
2nd	5000rpm	60sec	2nd	1500rpm	60sec

Step6: To put the ITO glass on the hot-plate and bake it for 1 hour at 200°C.

Step7: To rub the ITO glass with rubbing machine, the parameter of rubbing strength is used as below:

50%wt. Polyimide		2.5%wt. PVA	
Pile impression	0.2mm	Pile impression	0.23mm
Rotation rate	300rpm	Rotation rate	300rpm

Advancing rate	7.3mm/s	Advancing rate	7.3mm/s
----------------	---------	----------------	---------

Step8: To prepare 2.0 um of spacer, the small amount of spacer dropped six dots at the edge of bottom glass. Then, cover the top glass and press. Next, place the cell under a UV lamp for 5 minutes to fully cure and to measure a cell gap by using spectrometer UV-VIS 650 (from Perkin Elmer).

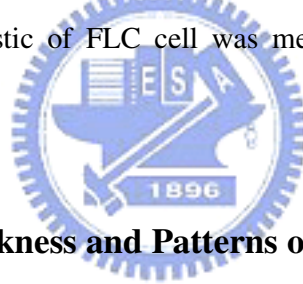
Step9: Heat up the FLC material until the temperature exceeded the clearing point.

Inject the FLC material into the empty cell until the FLC is full of the gap.

Step10: To anneal the FLC cell with programmable hot-plate, the annealing process depends on the phase sequence of the LC material.

Step11: To solder the wire at the top and bottom ITO by using ultrasonic soldering device (KURODA TECHNO Co., Ltd)

Step12: Then the characteristic of FLC cell was measured by using measurement instruments.



### **3.4 Observation of Thickness and Patterns of Thin-ITO Glasses**

#### **3.4.1 Observation of Thickness of Thin-ITO Glasses**

Thin-ITO was chose because of no grating effect. In order to confirm that the patterned electrodes were etched completely, the patterned-ITO glass has been etched at a long time and measured by AFM. So we could know accurately what the thickness of thin-ITO glasses is. Fig 3.3 shows that topographic images were obtained by scanning the boundary between ITO and etched-ITO regions. The results presents that the step height is 12.02nm. Therefore, all the etched patterned electrodes should be inspected according to the standard thickness.

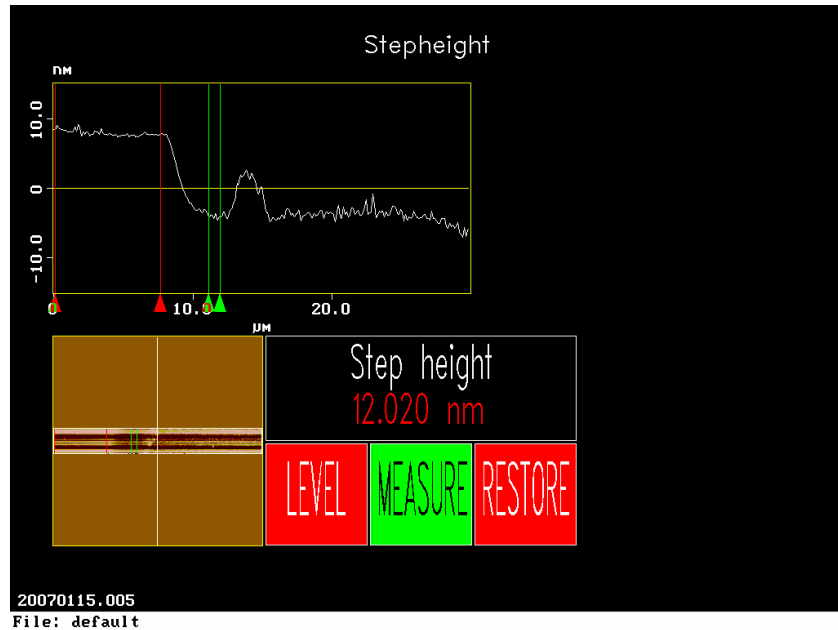


**Fig 3.3** The profile of non-ITO regions and ITO regions.

### 3.4.2 Observation of Etched and Overlapped-ITO Patterns

The 12nm thickness-ITO glasses were prepared and etched by the photolithographic technology. Etched-ITO patterns of 20um-period stripes and 40um-period stripes are presented as shows in Fig 3.4 (a) and (b).

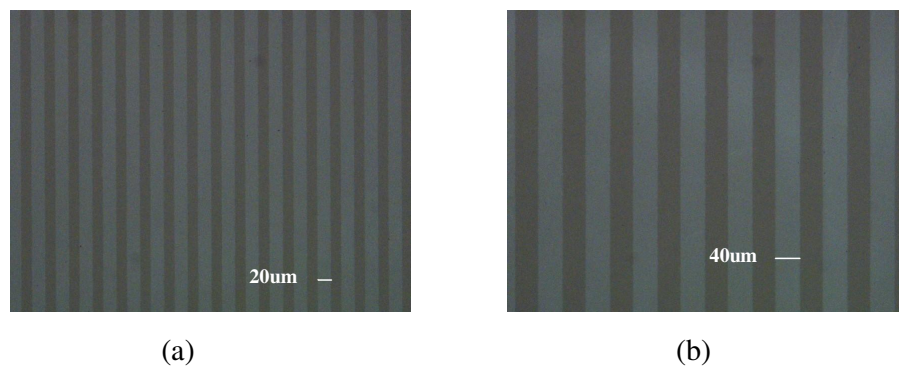


**Fig 3.4** POM textures shown: (a) 20um (b) 40um etched-ITO patterns

Each stripe is equal to each other for 20um-period strips or 40um-period strips. Two patterned-ITO glasses were observed and overlapped by POM as show in Fig 3.5 (a), overlapped-ITO patterns are shown on the top of another clearly and enlarged in order to confirm the alignment accuracy as show in Fig 3.5 (b).

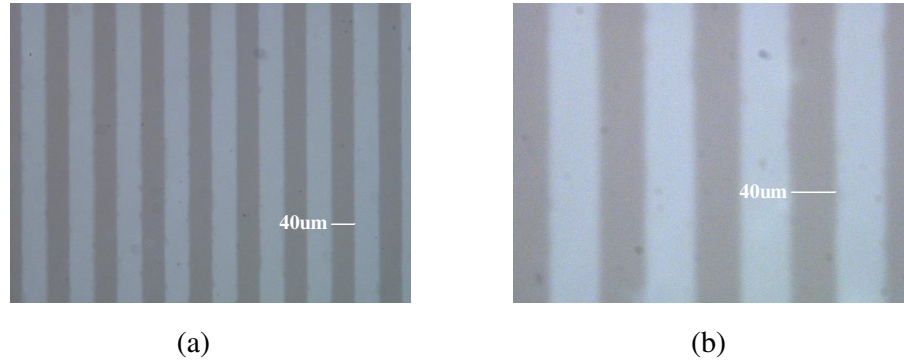
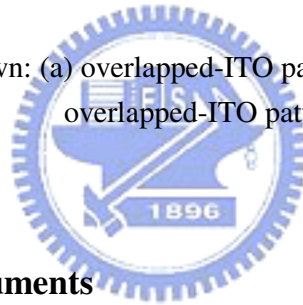


**Fig 3.5** POM textures shown: (a) overlapped-ITO patterns (b) the enlargement of overlapped-ITO patterns.



### 3.5 Measurement Instruments

#### 3.5.1 Atomic Force Microscope (AFM)

AFM consists of a scanning sharp tip at the end of a flexible cantilever across a sample surface while maintaining a small, constant force. The tips typically have an end radius of 2 nm to 20 nm, depending on tip type. The scanning motion is conducted by a piezoelectric tube scanner which scans the tip in a raster pattern with respect to the sample (or scans to the sample with respect to the tip). The tip-sample interaction is monitored by reflecting a laser off the back of the cantilever into a split photodiode detector. By detecting the difference in the photo-detector output voltages, changes in the cantilever deflection or oscillation amplitude are determined. A schematic diagram of this mechanism is depicted in Fig 3.6.

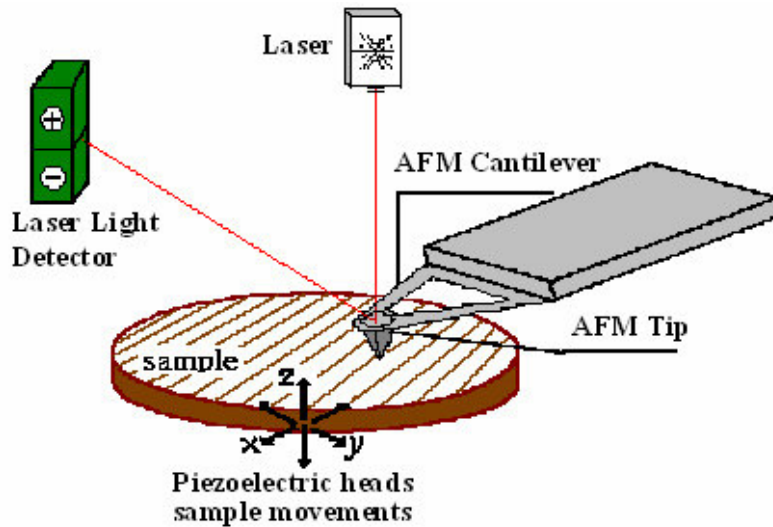


**Fig 3.6** Concept of AFM and the optical lever.

The two most commonly used modes of operation are contact mode AFM and TappingMode™ AFM, which are conducted in air or liquid environments. Contact mode AFM consists of scanning the probe across a sample surface while monitoring the change in cantilever deflection with the split photodiode detector. A feedback loop maintains a constant cantilever deflection by vertically moving the scanner to maintain a constant photo-detector difference signal. The distance the scanner moves vertically at each x, y data point is stored by the computer to form the topographic image of the sample surface. This feedback loop maintains a constant force during imaging, which typically ranges between 0.1 to 100 nN .

TappingMode AFM consists of oscillating the cantilever at its resonance frequency (typically ~300 kHz ) and lightly “tapping” on the surface during scanning. The laser deflection method is used to detect the root-mean-square (RMS) amplitude of cantilever oscillation. A feedback loop maintains a constant oscillation amplitude by moving the scanner vertically at every x, y data point. Recording this movement forms the topographical image. The advantage of TappingMode over contact mode is

that it eliminates the lateral, shear forces present in contact mode, enabling TappingMode to image soft, fragile, and adhesive surfaces without damaging them, which can be a drawback of contact mode AFM.

### 3.5.2 Cell Gap Measurement System

For liquid crystal display, the thickness of cell gap usually affects the optical performance. Especially for SSFLC, the suppressing of helical structure needs a very small cell gap and, in addition, the gap between the two alignment layers would also influence the orientation of FLC. Thus, every time before the infection of FLC we need to measure the empty cell gap, and interferometric method is what we use. The measurement instrument used is UV/Vis spectrometer LAMBDA 650 from Perkin Elmer, and the principle of this method is introduced as below.

The basic concept of the measurement method is based on the interference of light reflected by the two reflecting surfaces. The illustration is as Fig 3.7.  $R_1$ , a coefficient of reflection, is defined as ratio of the light reflected by surface 1 to the incident light.  $R_2$  is the reflection coefficient of surface 2.

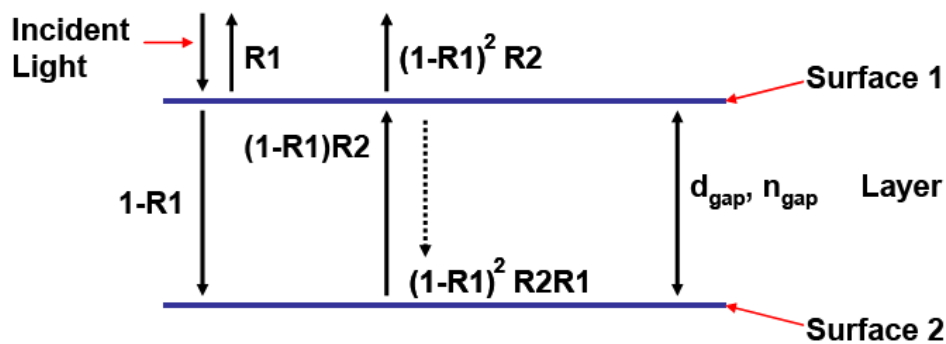


**Fig 3.7** Two reflecting surfaces separated by a layer causing a light interference. The dotted line indicates the first internal reflection.

If the total incident light is  $I = \cos \omega t$  and we assume there is no any absorption of light in surface 1 and 2, then we can write the total reflected light R as

$$R = R_1 \cos \omega t + \sum_{k=1}^{\infty} R_1^{k-1} R_2^k (1 - R_1)^{1+k} \cos \omega(t - kt_0) \quad (3-1)$$

Where  $\omega = 2\pi c n_{gap} / \lambda$  and  $t_0 = 2d_{gap} / c$ ,  $c$  is the speed of light in the vacuum,  $\lambda$  is the wavelength,  $d_{gap}$  is the thickness of the layer,  $n_{gap}$  is the refractive index of the layer. The cosine factor in Eq. (3-1) for  $k > 1$  are caused by internal reflections. Since  $R_1 < 1$  and  $R_2 < 1$ , the magnitude of the cosine factors for  $k > 1$  is much smaller than for  $k = 1$ . Therefore the internal reflection is chosen to be neglected, so

$$R = R_1 \cos \omega t + (1 - R_1)^2 R_2 \cos \left( \omega t - \frac{4\pi n_{gap} d_{gap}}{\lambda} \right) \quad (3-2)$$

Thus the reflected spectrum is

$$|R(\lambda)|^2 = R_1^2 + [(1 - R_1)^2 R_2]^2 + 2R_1(1 - R_1)^2 R_2 \times \cos(4\pi n_{gap} d_{gap} / \lambda) \quad (3-3)$$

The periodic term in Eq.(3-3) causes an interference pattern. The periodicity of the reflected interference spectrum determined the optical thickness of the cell gap,  $n_{gap} d_{gap}$ .

If  $\lambda_1$  and  $\lambda_2$  are the two wavelengths showing extrema in Eq.(3-3), then  $\cos(4\pi n_{gap} d_{gap} / \lambda) = \pm 1$  for  $\lambda = \lambda_1$  and  $\lambda = \lambda_2$ . Therefore

$$2n_{gap} d_{gap} = k_1 \lambda_1 / 2 \quad (3-4)$$

$$2n_{gap} d_{gap} = k_2 \lambda_2 / 2 \quad (3-5)$$

Where  $k_1$  and  $k_2$  are natural numbers. Suppose  $\lambda_1 > \lambda_2$ , then

$$k_2 = k_1 + x \quad (3-6)$$

Where  $x$  is a natural number.

Based on Eqs.(3-4), (3-5), and (3-6), we can write

$$n_{gap}d_{gap} = \frac{x\lambda_1\lambda_2}{4(\lambda_1 - \lambda_2)} \quad (3-7)$$

The value of  $x-1$  indicates the number of extrema in  $|R(\lambda)|^2$  between the wavelengths  $\lambda_1$  and  $\lambda_2$ . It is better to choose the distance  $x$  between the two extrema as large as possible for improving the accuracy of the calculation of  $n_{gap}d_{gap}$ .

The sample data was shown in Fig 3.8 for a 1.52 $\mu\text{m}$  cell.

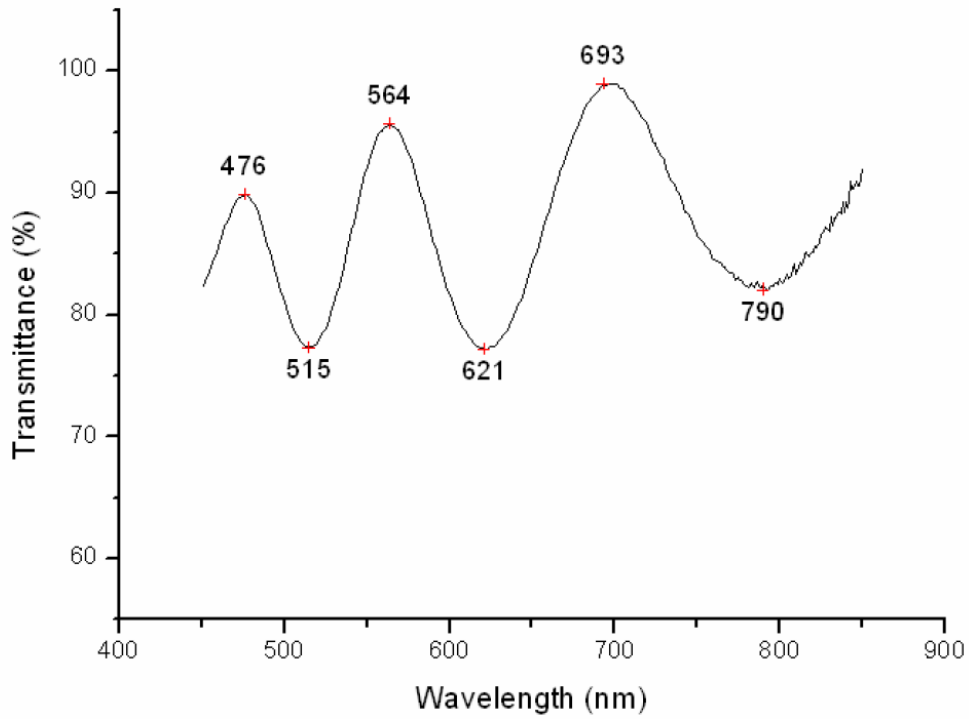


**Fig 3.8** Interference data of one Hybrid cell by UV-Visible.



### 3.5.3 Laser Optics Systems

Our laser optics system is as shown in Fig 3.9 This optical system is responsible for the measurement of electro-optical properties, such as V-T characteristics and response time. First of all, we have to reduce the intensity of laser source within the acceptable range of the photo detector by using a 10% ND filter. Three laser beams such as red, green, and blue wavelengths are prepared. We place the LC cell which is vertical, oblique, and parallel with the grating vector. The laser beam passes through the polarizer and then enters the LC cell. With applied voltage, the beam will be diffracted and received by the photo detector. The detector can be moved and changed any positions to measure the diffraction efficiency of one order. The driving waveform is written by ourselves and sent by a waveform generator WFG500 (from FLC Electronics AB).

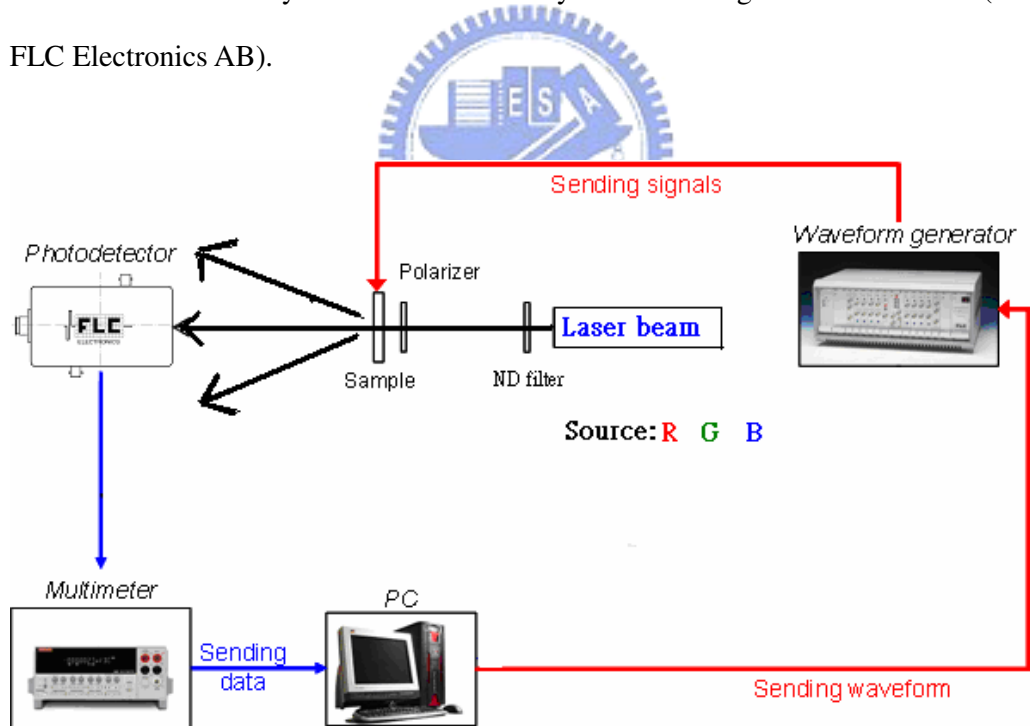


**Fig 3.9** A schematic diagram of the laser optics system.

### 3.5.4 Polarizing Optical Microscopy (POM)

The POM, OLYMPUS BX51 is as shown in Fig 3.10. Alignment textures were observed under POM with the magnifications of 100X, and the transparent mode is utilized with bottom light source. Next, the images were captured in the computer by CCD. Others application, distance and area can be calculated with its software.



**Fig 3.10** Instrument photo of POM.

## Chapter4

# Experimental Results and Discussion

### 4.1 Introduction of Experimental Objective

A novel ferroelectric liquid crystal phase grating has been successfully prepared by periodically ITO (indium-tin-oxide) patterned stripes cell. Under external driving voltage, LC molecules were reoriented in ITO areas and cause phase difference between the areas without ITO. The binary phase gratings were formed within periodically alternating domains. The R3206\_50% FLC material was suitable for liquid crystal phase grating application with the advantage of low driving voltage (5V). Alignment defects were suppressed by asymmetric hybrid cell, and the fringing field effect was reduced with low driving voltage. The response time of R3206\_50 was under 1.3ms in a 2.0um cell. Thus, a desirable fast switching, low driving voltage, high diffraction efficiency (25.8%) and easy process FLC grating was presented. Alignment textures by POM, surface properties by AFM, electro-optical properties and diffraction efficiencies by laser optics systems will be discussed in the concept.

## 4.2 Diffraction Efficiencies of 100nm-Thickness and 13nm-Thickness ITO Glasses

Two kinds thickness of ITO glasses were prepared in this research. Initially, the 100nm-thickness glass was used due to the standard glass for liquid-crystal materials. However, the glass was etched and formed grating patterns on itself. Then, after coating PI and LC injection, it would be found that the binary phase difference resulted in diffraction for the pattern-ITO glass as show in Fig 4.1. If an additional phase difference exist for any linear-polarizations, it was useless to be an ideal LC grating device. Because the two orthogonal polarizations both exist in the zero or the first order, they might not be separated completely into their own orders. In order to reduce the binary phase difference by the pattern-ITO glass, we chose 13nm-thickness glass. As a result, the slight phase difference almost not resulted in diffraction as show in Fig 4.1. Before demonstrating the device, thin-ITO glasses were achieved to be good performances for our research.

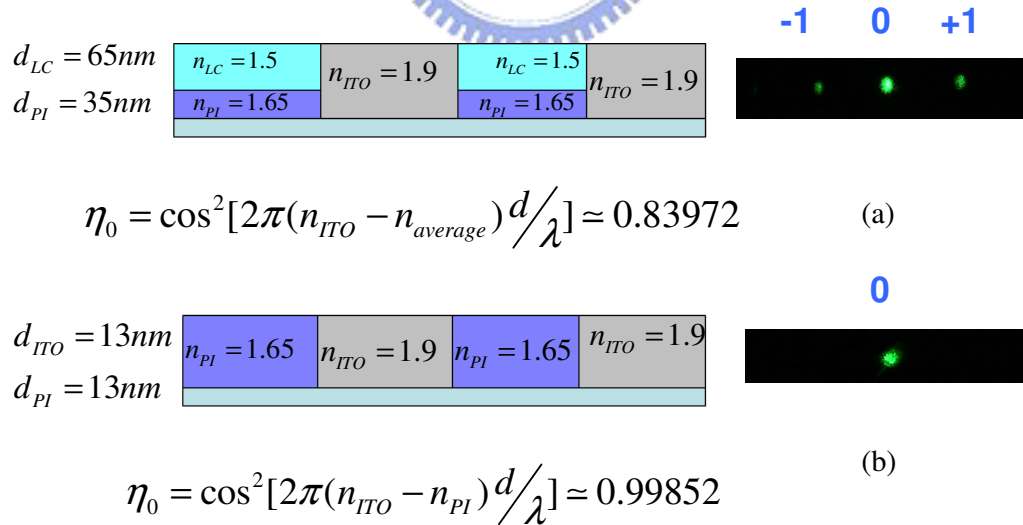


**Fig 4.1** Both diffraction efficiency and grating pattern are showed for (a) 100nm-thickness ITO glass and (b) 13nm-thickness ITO glass

### 4.3 Surface morphology

The results were shown in Fig 4.2 and Fig 4.3 by using Atomic Force Microscope (AFM). Topographic images were obtained by scanning an area of  $10 \times 10 \mu\text{m}^2$  for both samples. The mean roughness (Ra) of 50%wt. polyimide calculated with 1.945nm and the thickness of 50%wt. polyimide had 25nm. However, the mean roughness of PVA was smoother than 50%wt. polyimide with 1.742nm and the thickness of PVA had 95nm.

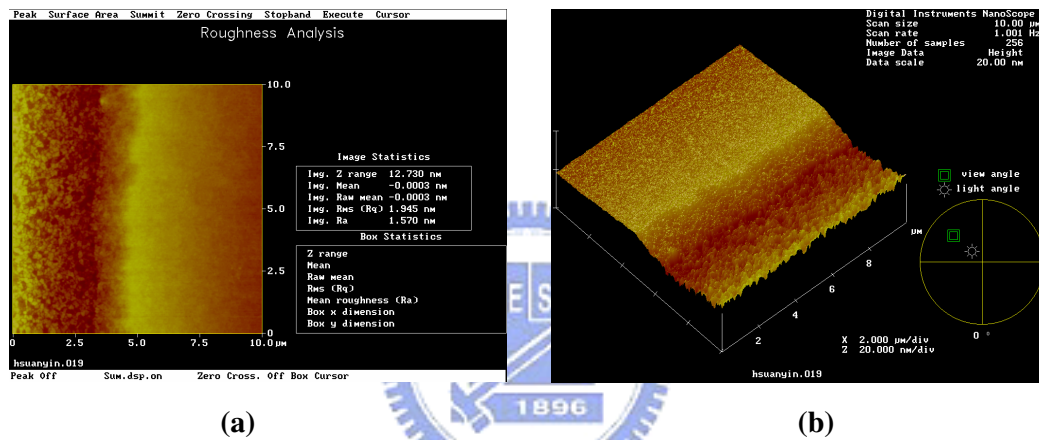


Fig 4.2 Surface morphology of 50 weight percentage polyimide (a) 2D (b) 3D

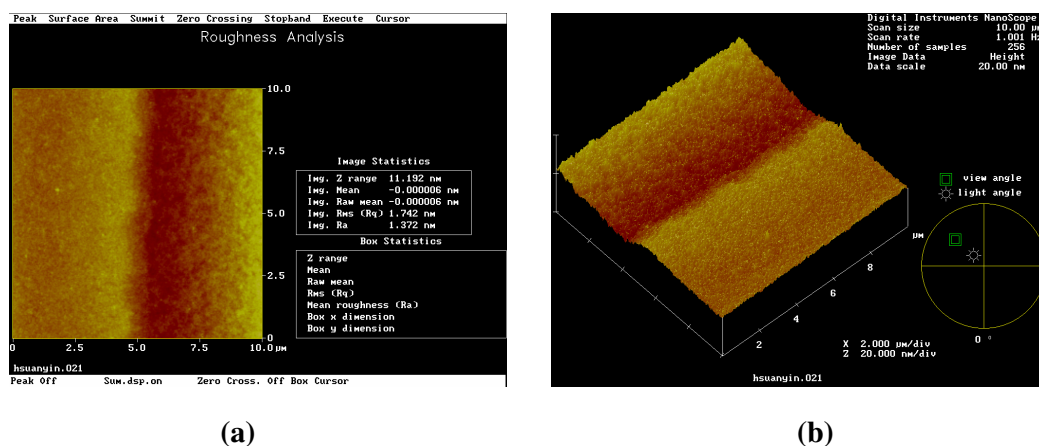


Fig 4.3 Surface morphology of 2.5 weight percentage PVA (a) 2D (b) 3D

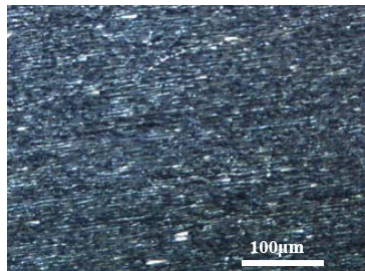
## 4.4 FLC Material (R3206-50) Distinctions

### 4.4.1 Alignment ability

In elastic-continuum energy theory, the FLC structures have uniform, helix and splay state. Besides, only uniform and helix state exist in the thin cell gap. From the pitch and cell gap relation, the free energy of uniform state is inversely proportional to the square of the pitch length while the free energy of helical state is independent of the pitch length. Therefore, the former will decrease and become smaller than the later with pitch length. The FLC molecular arrangement prefers to stay in uniform state, which is more stable at low energy.

LC alignment textures of R3206 and their mixtures in the same pre-made cell conditions were captured under POM. Pure R3206 showed poly-strip domain all over the sample. The diluted R3206 mixtures, on the other hand, showed larger domain size with less horizontal chevron defects as the weight percentage of R3206 lower than 50% as shown in Fig 4.4.

Asymmetrical hybrid alignment technique or asymmetrical cells eliminated alignment defects. Instead of liquid crystal polymers (LCPs) and linearly photo polymerized polymers (LPPs), poly vinyl alcohol (PVA) and polyimide (PI, from Chisso) were applied in this study. As show in Fig 4.5, the horizontal chevron defects of R3206\_50 were eliminated in hybrid cell. The alignment of R3206\_50 was greatly improved by the asymmetrical hybrid alignment cell approach compared to symmetric cell in Fig 4.4(b).



(a)



(b)

**Fig 4.4** Microscopic textures of alignment (a) R3206 (b) R3206\_50.

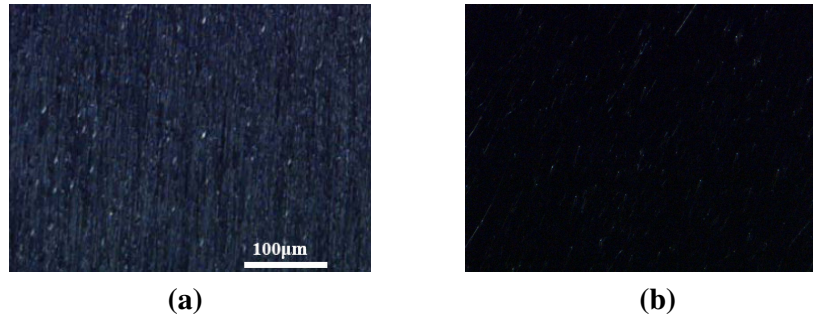


**Fig 4.5** Microscopic textures of alignment in hybrid cells.

#### 4.4.2 Electro-Optical Properties

Electro-optical properties were characterized by 100Hz square as presented in Fig 4.6. Half-V mode FLC materials R3206-50, possessing low driving voltage ( $V_{sat} = 5V$ ) was filled in a 2µm ITO-etched asymmetric hybrid cell. Response time of R3206-50 was characterized under 2µm hybrid cell, which presented extremely fast response (rise time: 380µs, fall time: 920µs) under 5V.

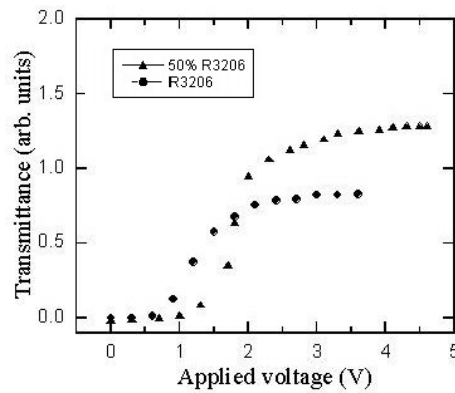


**Fig 4.6** Electro-optic properties of R3206 and R3206\_50 driven by 100Hz square



## 4.5 Experiment Part 1: The Period 20 $\mu$ m and 2 $\mu$ m Cell Gap

### 4.5.1 Grating Alignment Texture

Fig 4.7 shows the grating textures with applied different voltages for the period 20 $\mu$ m of grating patterns. The microscopic textures of our LC grating cell show an alternating microscopic striped texture observed at an angle of 45° between the grating vector and one of crossed polarizers. It was noted that the non-ITO regions presented the dark state due to non-retardation; the ITO regions presented the bright state due to phase retardation. Fig 4.7 (a) is shown that the width of dark stripes is equal to that of bright stripes with applied 3V. So we could explain that the electric field in the ITO regions was uniform and did not result in the fringing field behind 3V. However, when applied 5V, the width of dark stripes is not equal to that of bright stripes due to the fringing field as show in Fig 4.7 (b). As a result, diffraction efficiencies of the zero and the first order did not approach the theoretical limit for binary gratings.

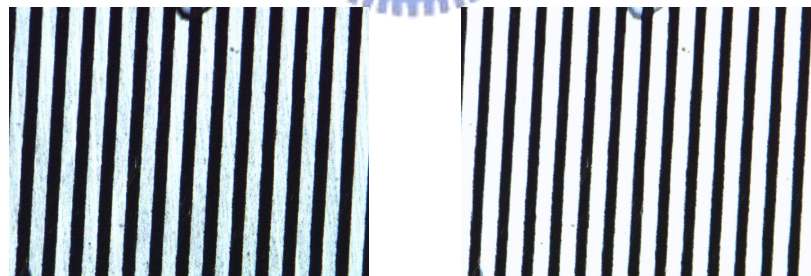


**Fig 4.7** Grating patterns investigated with POM and shown uniform periodically formed bright and dark regions at an angle of 45° between the grating vector and one of crossed polarizers by applied voltage: (a) 3V and (b) 5V.



## 4.5.2 Diffraction Efficiencies

Fig 4.8 shows a function of the zero-order and first-order diffraction efficiency-voltage with three wavelengths. For incident blue light, the first order has the maximum of  $\eta_{\pm 1} = 22.6\%$  at 5V, for incident green light, the first order has the maximum of  $\eta_{\pm 1} = 20\%$  at 5V and for incident red light, the first order has the maximum of  $\eta_{\pm 1} = 17.8\%$  at 5V. However, three values are not ideal values in this research because of the fringing field which results in the distortions in non-patterned-ITO.

According to Equation (2.9), diffraction efficiencies of the first order could be calculated and approach the results in Fig 4.8. At  $V_{\text{sat}}=5\text{V}$ , the curvature distortion resulted from fringing field inducing boundary distortions. Above concepts, several ways of reducing the fringing field are proposed.

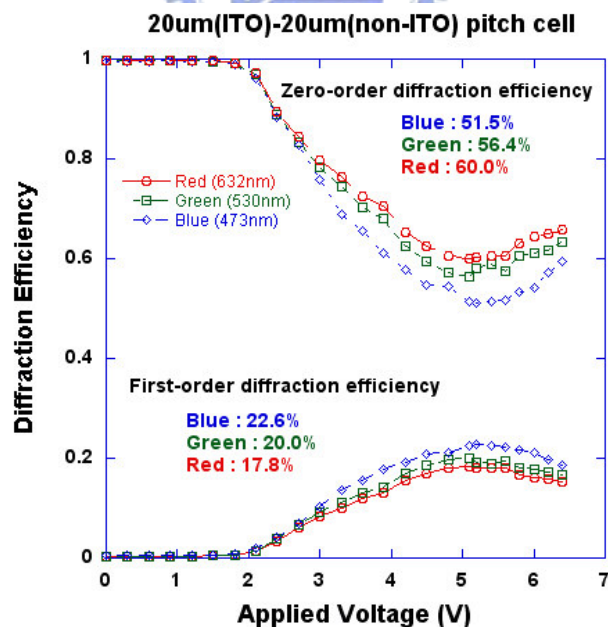


**Fig 4.8** Functions of the zero-order and first-order diffraction efficiency-voltage with three wavelengths.

## 4.6 Experiment Part 2: The Period 40um and 2um Cell Gap

### 4.6.1 Grating Alignment Texture

In the above-mentioned, the fringing field inducing boundary distortions of LC molecules at the edges of electrodes caused that widths of two states were not equal. In order to reduce the fringing field and achieve that widths of two states were equal accessibly, using of the longer period of patterned-ITO glasses was required. Fig 4.9 shows that an alternating microscopic striped texture observed at an angle of  $45^\circ$  between the grating vector and one of crossed polarizers. Widths of the dark and the bright states were also equal each other behind 3V. At 5V, the fringing field spread smaller regions on non-ITO regions, so the width of the dark stripe approached the width of the bright stripe.



**Fig 4.9** Grating patterns investigated with POM and shown uniform periodically formed bright and dark regions at an angle of  $45^\circ$  between the grating vector and one of crossed polarizers by applied voltage: (a) 3V and (b) 5V.

## 4.6.2 Diffraction Efficiencies

Fig 4.10 shows a function of the zero-order and first-order diffraction efficiency-voltage with three wavelengths. For incident blue light, the first order has the maximum of  $\eta_{\pm 1} = 23.2\%$  at 5V, for incident green light, the first order has the maximum of  $\eta_{\pm 1} = 22.4\%$  at 5V and for incident red light, the first order has the maximum of  $\eta_{\pm 1} = 20.8\%$  at 5V. Thus, three values are approached ideal values in this research because of the fringing field which results in the distortions in non-patterned-ITO.

According to Equation (2.9), diffraction efficiencies of the first order could be calculated and approach the results in Fig 4.10. At  $V_{\text{sat}}=5\text{V}$ , the fringing field effect reduced by using of the longer period of patterned-ITO glasses.

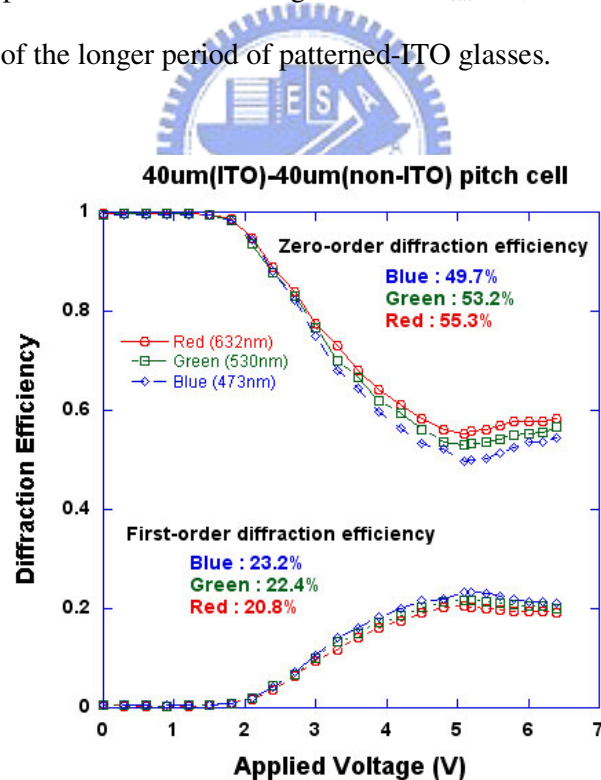


**Fig 4.10** Functions of the zero-order and first-order diffraction efficiency-voltage with three wavelengths.

## 4.7 Experiment Part 3: The Period 38-42um and 2um Cell Gap

### 4.7.1 Grating Alignment Texture

Fig 4.11 shows the grating textures with applied different voltages for the period 38-42um of grating patterns. Design the ITO region pitch was 38um and non-ITO region pitch was 42um, an ideal diffraction efficiency value is achieved by compensated the fringing field effect. The microscopic textures of our LC grating cell show an alternating microscopic striped texture observed at an angle of  $45^\circ$  between the grating vector and one of crossed polarizers. Fig 4.11 (a) is shown that the width of dark stripes is equal to that of bright stripes with applied 3V. Thus, when applied 5V, the fringing field effect was compensated by decreasing ITO region pitch glasses, the width of dark stripes is equal the bright stripes Fig 4.7 (b). As a result, first-order diffraction efficiencies were approached the theoretical limit for binary gratings.



**Fig 4.11** Grating patterns investigated with POM and shown uniform periodically formed bright and dark regions at an angle of  $45^\circ$  between the grating vector and one of crossed polarizers by applied voltage: (a) 3V and (b) 5V.

### 4.7.2 Diffraction Efficiencies

Fig 4.12 shows a function of the first-order diffraction efficiency-voltage with three wavelengths. For incident blue light, the first order has the maximum of  $\eta_{\pm 1} = 25.8\%$  at 5V, for incident green light, the first order has the maximum of  $\eta_{\pm 1} = 23.6\%$  at 5V and for incident red light, the first order has the maximum of  $\eta_{\pm 1} = 22.3\%$  at 5V. Thus, three values are approached ideal values in this research because of the fringing field was compensated in the not equal patterned-ITO pitch cell.

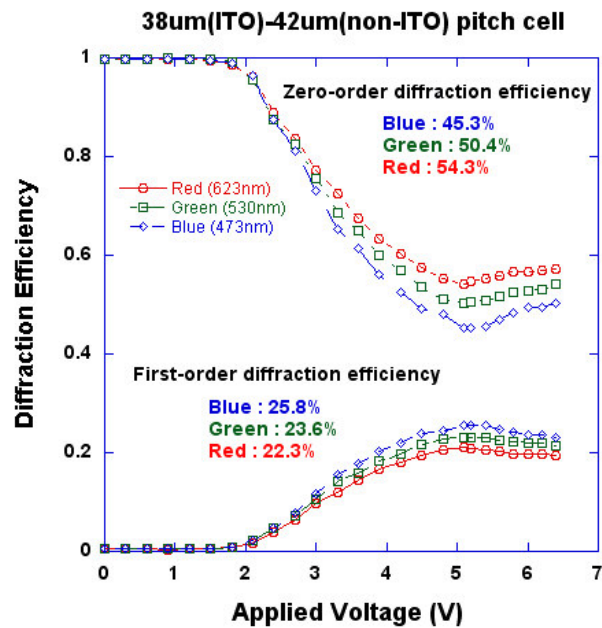


**Fig 4.12** Functions of the zero-order and first-order diffraction efficiency-voltage with three wavelengths.

# Chapter5

## Conclusions

### 5.1 Summary

A novel ferroelectric liquid crystal phase grating has been successfully prepared by periodically ITO (indium-tin-oxide) patterned stripes cell. Under external driving voltage, LC molecules were reoriented in ITO areas and cause phase difference between the areas without ITO. The binary phase gratings were formed within periodically alternating domains. Initially, the cell is illustrated no-diffraction without the applying field because of the slight phase difference arising from thin-thickness ITO glasses. In this study, FLC alignment defects were suppressed by asymmetric hybrid cell, and the fringing field effect was reduced with low driving voltage (5V) material (R3206-50). The response time of R3206-50 was under 1.3ms in a 2 $\mu$ m cell. Thus, a desirable fast switching, low driving voltage, high diffraction efficiency (25.8%), high contrast ratio and easy process mono-domain FLC grating was realized to be applied to optical communication, projection displays, optical switching and photonic liquid crystal devices.

### 5.2 Future Works

In the future, we maybe use a ferroelectric liquid crystal materials, which cone angle is 45°, to increase the phase retardation between two domains and to enhance diffraction efficiency. Besides, we use a multi-bistable FLC materials to achieves does not use the phase grating which the voltage actuates.

## Reference

- [1] T. Ajito, T. Obi, M. Yamaguchi and N. Ohyama, *Opt. Eng.*, 38 (2004)
- [2] J. Chen, P. J. Bos, H. Vithana and D. L. Johnson, *Appl. Phys. Lett.*, 67 (1995)
- [3] M. Bouvier and T. Scharf, *Opt. Eng.*, 2129 (2000)
- [4] J. A. Davis, J. Adachi, C. R. Fernandez-Pousa and I. Moreno, *Opt. Lett.*, 26 (2001)
- [5] S. Matsumoto, M. Goto, S. W. Choi, K. Ishikawa and H. Takezoe, *J. Appl. Phys.*, 99 (2006)
- [6] A. Y. G. Fuh and T. S. Mo, *Jpn. J. Appl. Phys.*, 41 (2002)
- [7] M. Honma and T. Nose, *J. Appl. Phys.*, 42 (2003)
- [8] A. Y. G. Fuh, T. S. Mo and C. H. Lin, *Jpn. J. Appl. Phys.*, 12 (2003)
- [9] N. A. Clark and S. T. Lagerwall, *Appl. Phys. Lett.*, 36 (1980)
- [10] N. Yamada, S. Kohzaki, F. Funada and K. Awane, *SID Digest*, 575 (1995)
- [11] A. Y. G. Fuh and T. S. Mo, *Mol. Cryst. Liq. Cryst.*, 413 (2004)
- [12] S. J. Woltman, J. N. Eakin and G. P. Crawford, *Opt. Lett.*, 22 (2006)
- [13] P. Janossy, *Opt. Lett.*, 17 (1992)
- [14] W. Gibbons and W. M. Shannon, *Nature*, 49 (1991)
- [15] G. P. Crawford, J. N. Eakin and M. D. Radcliffe, *J. Appl. Phys.*, 98 (2005)
- [16] J. N. Eakin, Y. Xie, R. A. Pelcovits, M. D. Radcliffe, G. P. Crawford, *Appl. Phys. Lett.*, 85 (2004)
- [17] H. Choi, J. W. Wu, H. J. Chang, B. Park, *Appl. Phys. Lett.*, 88 (2006)
- [18] G. Cipparrone, A. Mazzulla and G. Russo, *Appl. Phys. Lett.*, 78 (2001)
- [19] M. B. T. Scharf, *Opt. Lett.*, 39 (2000)
- [20] C. V. Brown, E. Kriezis and S. J. Elston, *J. Appl. Phys.*, 91 (2002)
- [21] S. P. Gorkhali and R. A. Pelcovits, *Appl. Phys. Lett.*, 88 (2006)

- [22] Z. Sekkat and M. Dumont, *Jpn. J. Appl. Phys.*, 54 (1994)
- [23] E. Hasman, Z. Bomzon and V. Kleiner, *Opt. Commun.*, 209 (2002)
- [24] P. T. Lin, X. Liang, H. Ren and S. T. Wu, *Appl. Phys. Lett.*, 85 (2004)
- [25] H. Choi, J. W. Wu, H. J. Chang and B. Park, *Appl. Phys. Lett.*, 88 (2006)
- [26] D. Subacius, J. E. Stockley and S. A. Serati, *SPIE Proceedings*, 3778 (1999)
- [27] N. Manabe, M. Inoue and J. Akanowatari, *AM-LCD IDW*, 96 (1996)
- [28] B. O. Myrvold, *Liq. Cryst.*, 637 (1989)
- [29] B. O. Myrvold, *Liq. Cryst.*, 261 (1990)
- [30] J. Kanbe, H. Inoue, A. Mizutome, Y. Hanyuu and S. Yoshihara, *Ferroelectrics*, 114 (1991)
- [31] N. A. Clark and S. T. Lagerwall, *Appl. Phys. Lett.*, 36 (1980)
- [32] T. P. Rieker, N. A. Clark, G. S. Smith, D. S. Parmar, E. B. Sirota and C. R. Safinya, *Phys. Rev. Lett.*, 59 (1987)
- [33] Y. Asao, T. Togano, M. Terada, T. Moriyama and S. Nakamura, *Jpn. J. Appl. Phys.*, 38 (1999)
- [34] M. Koden, T. Numao, N. Itoh, M. Shiomi and T. Wada, *Proc. Japan Display*, 519 (1992)
- [35] A. Tsuboyama, Y. Hanyuu, S. Yoshihara and J. Kanbe, *Proc. Japan Display*, 53 (1993)
- [36] Y. Sato, T. Tanaks, H. Kobayashi, K. Aoki, H. Watanable, T. Takeshita, T. Ouchi, H. Takezoe and A. Fukuda, *Jpn. J. Appl. Phys.*, 28 (1989)
- [37] A. Mochizuki, K. Motoyoshi and M. Nakatsuka, *Ferroelectrics*, 37 (1991)
- [38] T. Nonaka, J. Li, A. Ogawa, B. Hornung, W. Schmidt, R. Wingen and H. R. Duebal, *Liq. Cryst.*, 26 (1999)
- [39] T. Furukawa, M. Shigeta, H. Uchida and M. Koden, *Proc. IDW*, 251 (2000)
- [40] B. O. Myrvold, *Ferroelectrics*, 85 (1988)



- [41] J. Dijon, C. Ebel and L. Mulatier, *Ferroelectrics*, 47 (1988)
- [42] K. Takatoh, H. Nagata and T. Saishu, *Ferroelectrics*, 173 (1996)
- [43] J. A. Davis and J. Adachi, *Opt. Lett.*, 26 (2001)
- [44] J. A. Davis and J. Adachi, *Opt. Lett.*, 29 (2004)
- [45] B. Apter, U. Efron and E. B. Treidel, *Opt. Lett.*, 43 (2004)
- [46] S. Matsumoto and G. Kawamura, *J. Appl. Phys.*, 99 (2006)

